

Viscous erosion with a generalized traction integral equation

William H. Mitchell and Saverio E. Spagnolie

Department of Mathematics, University of Wisconsin-Madison, 480 Lincoln Dr., Madison, WI 53706

(Dated: July 28, 2022)

A double-layer integral equation for the surface tractions on a body moving in a viscous fluid is derived, allowing for the incorporation of a background flow and/or the presence of a plane wall. The Lorentz reciprocal theorem is used to link the surface tractions on the body to integrals involving the background velocity and stress fields on an imaginary bounding sphere (or hemisphere for wall-bounded flows). The derivation requires the velocity and stress fields associated with numerous fundamental singularity solutions which we provide for free-space and wall-bounded domains. Two sample applications of the method are discussed: we study the tractions on an ellipsoid moving near a plane wall, which provides a more detailed understanding of the well-studied glancing and reversing trajectories, and we explore a new problem, erosion of bodies by a viscous flow, in which the surface is ablated at a rate proportional to the local viscous shear stress. Simulations and analytical estimates suggest that a spherical body in a uniform flow first reduces to nearly (but not exactly) the drag minimizing profile of a body in a Stokes flow and then vanishes in finite time. The shape dynamics of an eroding body in a shear flow and near a wall are also investigated. Stagnation points of the flow on the body lead generically to the formation of cusps, whose number depends on the flow configuration and/or the presence of a nearby wall.

I. INTRODUCTION

Fluid-body interactions at microscopic length scales or in highly viscous flows are of common interest in physics, biology, and engineering. Of fundamental interest in such systems is the distribution of force per unit area, or traction, on an immersed body as it moves through the fluid. Distributions of surface tractions also play critical roles in numerous biological processes, including significantly affecting the structure, formation, and detachment of biofilms [1–5]. The competition between surface tractions and bacterial adhesion has numerous consequences for human health [6], for instance in microcirculation [7] where fluid shear stress can cause changes in endothelial cell fluidity [8] and cell turnover rates [9], and where it can affect platelet adhesion [10]. Plaque rupture and erosion are also shear-stress dependent [11, 12]. Techniques for measuring elastic moduli of cells depend on theoretical relations between shear stress and membrane properties [13] which could be refined with a more detailed understanding of stress distribution on the cell surface. If the particle is soft, surface tractions may result in changes of the body shape and trajectory [14, 15], from the dynamics of flexible filaments [16–22] and vesicles [23–27] to the shapes of single [28–31] and many [32–37] red blood cells in flow. The shapes of cells and membranes in flow are determined by a balance between viscous tractions and elastic membrane forces [28] including the lifting of vesicles near walls by shear flows [24, 38, 39].

Viscous tractions also enable biolocomotion. Microorganisms use flagellar undulations, ciliary wave propagation, and other mechanisms to generate tractions which propel them through the fluid [40]. A common modeling approach in ciliary locomotion and mucus transport alike is to treat the layer of ciliary actuation as a smooth traction surface [41–43]. Distribution of traction is important for efficient locomotion [44] as it enters locally into the description of the required power [40, 45]. The presence of walls can reduce the effectiveness of a given ciliary traction, resulting in slower swimming speeds of *Paramecia* near surfaces [46–48]. Placement of actuation precisely where fluid stress is extremal in the mobility problem can be used to optimize swimming speeds in viscous flows [49].

In other contexts surface tractions may result in local material loss, leading to the selection of certain eroding body geometries [50–52]. At large length and velocity scales, mass transfer can be influenced heavily by background flows in dissolution [53–56] and melting [57, 58]. At smaller length scales there are important applications in chemical and industrial engineering, and geophysics, from mass transfer from one

or two spheres, cylinders, or bodies of revolution [59–64], to more general shapes and finer-scale details [65–67]. Among other pharmaceutical applications are hydrodynamic manipulation of dissolution for drug-delivery purposes [68–74].

There have been numerous efforts to determine surface tractions in zero Reynolds number¹ (Stokes) flows. Methods based on integral equations are attractive because of the associated dimension reduction. Such techniques can be classified in several ways: according to whether a first- or second-kind Fredholm integral equation [75] is solved; whether or not the nullspace of the integral operator is trivial; by the type of discontinuity encountered in the integrands; whether the traction vectors are obtained directly from the linear system or indirectly from a secondary variable; and finally according to simplicity of derivation and implementation.

The earliest relevant works used first-kind integral formulations; in many cases these methods enjoyed some success despite the ill-posedness of the continuous problem and associated conditioning issues in discretizations [76]. Second-kind formulations emerged later, likely because of the impossibility of representing an arbitrary Stokes flow using the double-layer potential alone. An important step forward occurred in 1987 when Power and Miranda used a double-layer potential together with a *completion flow* to represent the velocity exterior to a particle [77]. The completion flow is capable of exerting an arbitrary finite force and torque on the particle; the inclusion of this flow remedies the rank deficiency of the double-layer integral operator. We follow [78] in referring to this method, as generalized and refined in [79], as the *completed double-layer boundary integral equation* or CDLBIE.

As a method for determining fluid velocities and the net force and torque on suspended particles, the CDLBIE has been very successful. Where surface tractions are required, several methods have been proposed. Kim and Karrila used a Riesz reciprocal theorem argument and the CDLBIE to derive a second-kind integral equation for the tractions on rigid particles in a quiescent fluid [79]. This equation is known as the *completed traction boundary integral equation* or CTBIE. If one accepts the restriction to rigid motions, the CTBIE has all of the properties identified as being desirable above. Moreover, the derivation of the CTBIE using the Riesz lemma is admirably concise [78]. Liron and Barta obtained another second-kind traction integral equation by differentiating the single-layer velocity field [80], although this leads to a noninvertible integral operator which then needs to be completed after the fact. Ingber and Mondy gave a third traction integral equation [81]; their formulation involves hypersingular integrals, which the authors mitigate by presenting a regularization procedure. In most of the pointwise traction computations carried out in the literature the fluid is assumed to be at rest at infinity; one exception is an effort by Pozrikidis who studied shear flow over a protuberance on a wall using a first-kind integral equation [82].

In this work we present an integral equation for determining the surface tractions on a rigid body immersed in a Stokes flow which incorporates the effect of a background flow and/or the presence of a nearby wall. The Lorentz reciprocal theorem is used to link the surface tractions on the body to integrals involving the background velocity and stress fields on an imaginary bounding sphere (or hemisphere for wall-bounded flows). The formulation reduces to an especially simple form when the background flow is linear and the radius of the bounding surface is taken to infinity. The method requires the velocity and stress fields associated with numerous fundamental singularity solutions, and various integrals including these fields, which we provide for free-space and wall-bounded domains. The inclusion of a background flow is shown to alter only the right-hand side of the system whereas the inclusion of a no-slip plane wall affects only the integral operator. Two sample applications are discussed. First, the method is used to compute the pointwise traction on a spheroidal body as it sediments under the influence of gravity near a no-slip wall, which provides a more detailed understanding of well-studied glancing and reversing trajectories. Second, we explore a new problem, the erosion of bodies by a viscous flow, in which the surface is ablated at a rate proportional to the local viscous shear stress. Simulations and analytical estimates suggest that a spherical body in a uniform flow first reduces to nearly (but not exactly) the drag minimizing profile of a body in a Stokes flow and then

¹ The Reynolds number is defined by $Re = \rho UL/\mu$, where ρ is the fluid density, μ is the viscosity, and U and L are characteristic velocity and length scales in the problem.

Velocity	Pressure	Stress
$G_{ij} = \frac{\delta_{ij}}{R} + \frac{X_i X_j}{R^3},$	$G_j^P = 2 \frac{X_j}{R^3},$	$G_{ijm}^{STR} = -6 \frac{X_i X_j X_m}{R^5}$
$R_{ij} = \frac{\epsilon_{ijp} X_p}{R^3},$	$R_j^P = 0,$	$R_{ijm}^{STR} = -3 \frac{\epsilon_{ijp} X_m X_p + \epsilon_{mjp} X_i X_p}{R^5}$
$T_{ijk} = -6 \frac{X_i X_j X_k}{R^5},$	$T_{jk}^P = 4 \frac{\delta_{jk}}{R^3} - 12 \frac{X_j X_k}{R^5},$	$T_{ijk}^{STR} = -4 \frac{\delta_{im} \delta_{jk}}{R^3} - 6 \frac{\delta_{jm} X_i X_k + \delta_{km} X_i X_j + \delta_{ij} X_k X_m + \delta_{ik} X_j X_m}{R^5} + 60 \frac{X_i X_j X_k X_m}{R^7}$

TABLE I. Formulas for the Stokeslet, rotlet, and stresslet in an unbounded fluid, each with an associated velocity, pressure, and stress field. Here $\mathbf{X} = \mathbf{x} - \mathbf{y}$, $R = |\mathbf{X}|$, δ_{ij} denotes the identity operator and ϵ_{ijk} is the alternating tensor or Levi-Civita symbol.

vanishes in finite time. The shape dynamics of an eroding body in a shear flow and near a wall are also investigated. Stagnation points of the flow on the body lead generically to the formation of cusps, whose number depends on the flow configuration and/or the presence of a nearby wall.

The paper is organized as follows. After some preliminaries in §II, the new integral equations are derived in §III and a discretization strategy suitable for treating particles of arbitrary shape is described in §IV. Applications are the topic of §V; namely, the traction fields on sedimenting particles near no-slip walls are computed and discussed in §V A, and simulations of eroding particles in uniform and shear flows are performed in section §V B, with an accompanying analysis. We conclude with a discussion in §VI.

II. PRELIMINARIES

The Stokes equations of viscous flow, valid for vanishingly small Reynolds numbers, are given by

$$-\nabla p + \mu \nabla^2 \mathbf{u} = \mathbf{0}, \quad (1)$$

$$\nabla \cdot \mathbf{u} = 0, \quad (2)$$

where \mathbf{u} is the velocity field, p is the pressure, and μ is the viscosity [83]. The linearity of the Stokes equations enables the use of powerful techniques associated with Green's functions. In this section we discuss three of these singular solutions and collect some useful properties, including two formulas concerning the *double-layer potential* or distribution of stresslet velocities.

In any geometry, the *Stokeslet* or *Lorentzlet*² is defined as the solution of

$$-\nabla p + \mu \nabla^2 \mathbf{u} = -\delta(\mathbf{x} - \mathbf{y}) \mathbf{f}, \quad (3)$$

$$\nabla \cdot \mathbf{u} = 0, \quad (4)$$

where $\delta(\mathbf{x} - \mathbf{y}) \mathbf{f}$ is a point force, \mathbf{y} is the *source point*, and all derivatives are with respect to \mathbf{x} . As the system is linear, the velocity, pressure, and stress fields associated with the point force are obtained by

² The term *Lorentzlet* is not in current use, but this is a little unfair to H. A. Lorentz, who employed this tensor as early as 1896 despite some initial misgivings about the unbounded velocity near the source point; see the exposition by Kuiken [84] on Lorentz's original paper [85].

contracting tensors G , G^P , and G^{STR} , respectively, against constant multiples of \mathbf{f} :

$$u_i(\mathbf{x}) = \frac{1}{8\pi\mu} G_{ij}(\mathbf{x}, \mathbf{y}) f_j, \quad (5)$$

$$p(\mathbf{x}) = \frac{1}{8\pi} G_j^P(\mathbf{x}, \mathbf{y}) f_j, \quad (6)$$

$$\sigma_{ik}(\mathbf{x}) = \frac{1}{8\pi} G_{ijk}^{STR}(\mathbf{x}, \mathbf{y}) f_j. \quad (7)$$

If the fluid is unbounded these tensors take simple forms; they are provided in Table I (see [86]). Fundamental *rotlet* tensor solutions R , R^P , R^{STR} , associated instead with a point torque in the fluid, have associated velocity $R_{ij}L_j/(8\pi\mu)$, pressure $R_j^PL_j/(8\pi)$, and stress $R_{ijk}^{STR}L_j/(8\pi)$ (see Table I). Finally, a *stresslet* solution, so named because its velocity field in free space arises upon two contractions with the Stokeslet stress tensor G_{ijk}^{STR} , is a Stokes flow solution with velocity, pressure, and stress given by

$$u_i(\mathbf{x}) = \frac{1}{8\pi} T_{ijk}(\mathbf{x}, \mathbf{y}) s_{jk}, \quad (8)$$

$$p(\mathbf{x}) = \frac{\mu}{8\pi} T_{jk}^P s_{jk}, \quad (9)$$

$$\sigma_{im}(\mathbf{x}) = \frac{\mu}{8\pi} T_{ijkm}^{STR}(\mathbf{x}, \mathbf{y}) s_{jk}, \quad (10)$$

such that $T_{ijk} = G_{ijk}^{STR}$. The units of s_{jk} are area times velocity; in this paper $s_{jk} = \psi_j n_k$ always has rank one. Algebraic expressions for all of these tensors appear in Table I for an unbounded fluid. Half-space solutions may be obtained from the free-space versions by the addition of image systems which result in a no-slip plane wall; these image systems may be derived using the reflection principle of Lorentz, as described in Appendix A. The half-space tensors for the velocity, pressure, and stress fields above are included as Table III.

A *double-layer potential* is a velocity field formed from a distribution of stresslets over a closed surface,

$$u_i^{DL}(\mathbf{x}) = \frac{1}{8\pi} \int_D T_{ijk}(\mathbf{x}, \mathbf{y}) \psi_j(\mathbf{y}) n_k(\mathbf{y}) dS_{\mathbf{y}}. \quad (11)$$

Here ψ is an arbitrary density function with units of velocity, and the normal vector, as throughout the paper, points out of the body surface into the fluid domain. The velocity field (11) is smooth in the interior and exterior of D but has a bounded jump discontinuity across D .

In the remainder of this section we will demonstrate two useful identities concerning double-layer potentials. The first of these gives the tensor resulting when ψ_j is omitted from the integrand in (11). The value depends on whether the observation point \mathbf{x} lies within, exterior to, or on the distribution boundary D . By the definition of the stresslet and (4), we have $(\partial/\partial x_k)T_{ijk}(\mathbf{x}, \mathbf{y})/8\pi = -\delta_{ij}\delta(\mathbf{x} - \mathbf{y})$. The divergence theorem then gives the identity we seek:

$$\frac{1}{8\pi} \int_D T_{ijk}(\mathbf{x}, \mathbf{y}) n_k(\mathbf{y}) dS_{\mathbf{y}} = -\delta_{ij} \int_V \delta(\mathbf{x} - \mathbf{y}) dV_{\mathbf{y}} = \begin{cases} 0 & \mathbf{x} \text{ exterior to } D \\ -\delta_{ij} & \mathbf{x} \text{ interior to } D \\ -\delta_{ij}/2 & \mathbf{x} \text{ on } D. \end{cases} \quad (12)$$

The second formula we wish to establish gives the limiting value of the double-layer potential as the observation point \mathbf{x}^e approaches a point \mathbf{x} on the distribution surface D from the exterior side of D . The

argument uses first the exterior case and then the boundary case in (12):

$$\begin{aligned}
\lim_{x^e \rightarrow x} \frac{1}{8\pi} \int_D T_{ijk}(x^e, \mathbf{y}) n_k(\mathbf{y}) \psi_j(\mathbf{y}) dS_{\mathbf{y}} - 0 &= \lim_{x^e \rightarrow x} \frac{1}{8\pi} \int_D T_{ijk}(x^e, \mathbf{y}) n_k(\mathbf{y}) [\psi_j(\mathbf{y}) - \psi_j(x)] dS_{\mathbf{y}} \\
&= \frac{1}{8\pi} \int_D T_{ijk}(x, \mathbf{y}) n_k(\mathbf{y}) [\psi_j(\mathbf{y}) - \psi_j(x)] dS_{\mathbf{y}} \\
&= \frac{1}{8\pi} \int_D T_{ijk}(x, \mathbf{y}) n_k(\mathbf{y}) \psi_j(\mathbf{y}) dS_{\mathbf{y}} + \frac{1}{2} \psi_i(x).
\end{aligned} \tag{13}$$

The evaluation of the limit is legitimate because of the regularity provided by the extra zero factor $(\psi_j(\mathbf{y}) - \psi_j(x))$; for more details see the book by Pozrikidis [86]. Both equations (12) and (13) will be employed below.

III. GENERALIZED TRACTION INTEGRAL EQUATIONS

We now show how the argument presented in [78] can be extended to solve the resistance problem with nonzero background flow and/or a no-slip plane wall. We find that the background flow affects the right-hand side of the system but not the integral operator, whereas the presence of a plane wall affects the integral operator but not the right-hand side. The corresponding mobility problems are discussed later.

A. A background flow in free space

Let D denote the boundary of a rigid particle immersed in an unbounded fluid with centroid \mathbf{Y} , and let S denote a sphere of large radius centered at the origin and containing the particle. The Lorentz reciprocal theorem states that two Stokes solutions with velocity and stress fields $(\mathbf{u}, \boldsymbol{\sigma})$ and $(\mathbf{u}', \boldsymbol{\sigma}')$ satisfy [86, 87]:

$$\nabla \cdot (\mathbf{u}' \cdot \boldsymbol{\sigma} - \mathbf{u} \cdot \boldsymbol{\sigma}') = 0. \tag{14}$$

Integrating the above over a volume bounded by D and S , and applying the divergence theorem, we have

$$\langle \mathbf{u}', \mathbf{f} \rangle_D + \langle \mathbf{u}', \mathbf{f} \rangle_S = \langle \mathbf{u}, \mathbf{f}' \rangle_D + \langle \mathbf{u}, \mathbf{f}' \rangle_S, \tag{15}$$

where \mathbf{f} and \mathbf{f}' are the surface tractions exerted by the flows \mathbf{u} and \mathbf{u}' , respectively, and $\langle \mathbf{u}', \mathbf{f} \rangle_D = \int_D \mathbf{u}' \cdot \mathbf{f} dS$. The first solution $(\mathbf{u}, \boldsymbol{\sigma})$ will solve the resistance problem of principal interest: the flow \mathbf{u} arises when the body moves with specified velocity \mathbf{U} and rotation vector $\boldsymbol{\Omega}$ in a fluid with specified background flow/pressure fields $\mathbf{u}^\infty, p^\infty$. It is the surface tractions \mathbf{f} associated with this flow that we ultimately seek. Boundary conditions for \mathbf{u} are given by the no-slip boundary condition on D , $\mathbf{u} = \mathbf{U} + \boldsymbol{\Omega} \times (\mathbf{x} - \mathbf{Y})$, and by decay towards the background flow field at infinity, $|\mathbf{u} - \mathbf{u}^\infty| = O(1/|\mathbf{x} - \mathbf{Y}|)$ as $|\mathbf{x} - \mathbf{Y}| \rightarrow \infty$. The power of the reciprocal theorem becomes apparent upon the selection of the second, auxiliary solution. Let \mathbf{u}' denote a velocity field consisting of the sum of a double-layer potential and a *completion flow*; specifically, for \mathbf{x} in the exterior of the body we define

$$\mathbf{u}'_i(\mathbf{x}) = \frac{1}{8\pi} \int_D T_{ijk}(x, \mathbf{y}) n_k(\mathbf{y}) \psi_j(\mathbf{y}) dS_{\mathbf{y}} + \frac{c}{8\pi} \int_D C_{ij}(x, \mathbf{y}) \psi_j(\mathbf{y}) dS_{\mathbf{y}}, \tag{16}$$

where \mathbf{n} is the normal vector pointing into the fluid from the particle, T_{ijk} is the free-space stresslet, and ψ is an arbitrary smooth vector field on D with units of velocity. The proportionality constant c and the tensor C_{ij} both have units of inverse length. The completion flow is required to be regular both on and exterior to D , and moreover it must exert a total force and torque $\mathbf{F} = c\mu \int_D \psi(\mathbf{y}) dS_{\mathbf{y}}$ and $\mathbf{L} = c\mu \int_D (\mathbf{y} - \mathbf{Y}) \times \psi dS_{\mathbf{y}}$ on the particle. The completion flow can be specified in several ways; later we will consider a specific choice

but for now we leave the expressions general for the benefit of others who may wish to use a different completion flow. The purpose of including the completion flow is to complete the range of the integral operator, since the double layer potential alone is incapable of exerting a net force or torque on the particle [86].

The next step is to write all four integrals in (15) as inner products against ψ . Two of the terms have been discussed elsewhere [78, 79]; we include the arguments here for completeness. For the term $\langle \mathbf{u}', \mathbf{f} \rangle_D$, we need an expression for the double layer potential in the limit where the observation point \mathbf{x}^e approaches a boundary point $\mathbf{x} \in D$ from the exterior, i.e. (13). Using this we obtain

$$\begin{aligned} \langle \mathbf{u}', \mathbf{f} \rangle_D &= \int_D f_i(\mathbf{x}) \left[\frac{1}{2} \psi_i(\mathbf{x}) + \frac{1}{8\pi} \int_D T_{ijk}(\mathbf{x}, \mathbf{y}) n_k(\mathbf{y}) \psi_j(\mathbf{y}) dS_y + \frac{c}{8\pi} \int_D \psi_j(\mathbf{y}) C_{ij}(\mathbf{x}, \mathbf{y}) dS_y \right] dS_x \\ &= \int_D f_i(\mathbf{x}) \int_D \psi_j(\mathbf{y}) \left[\frac{1}{2} \delta_{ij} \delta(\mathbf{x} - \mathbf{y}) + \frac{1}{8\pi} T_{ijk}(\mathbf{x}, \mathbf{y}) n_k(\mathbf{y}) + \frac{c}{8\pi} C_{ij}(\mathbf{x}, \mathbf{y}) \right] dS_y dS_x \\ &= \int_D \psi_j(\mathbf{y}) \left[\frac{1}{2} f_j(\mathbf{y}) + \frac{n_k(\mathbf{y})}{8\pi} \int_D T_{ijk}(\mathbf{x}, \mathbf{y}) f_i(\mathbf{x}) dS_x + \frac{c}{8\pi} \int_D C_{ij}(\mathbf{x}, \mathbf{y}) f_i(\mathbf{x}) dS_x \right] dS_y. \end{aligned} \quad (17)$$

For the term $\langle \mathbf{u}, \mathbf{f}' \rangle_D$, we use the fact that \mathbf{u} is a rigid body motion, along with the relations between ψ and (\mathbf{F}, \mathbf{L}) assumed above, resulting in:

$$\langle \mathbf{u}, \mathbf{f}' \rangle_D = \langle \mathbf{U} + \boldsymbol{\Omega} \times (\mathbf{y} - \mathbf{Y}), \mathbf{f}' \rangle_D = \mathbf{U} \cdot \mathbf{F} + \boldsymbol{\Omega} \cdot \boldsymbol{\tau} = \langle c\mu \mathbf{U} + c\mu \boldsymbol{\Omega} \times (\mathbf{y} - \mathbf{Y}), \psi \rangle_D. \quad (18)$$

If there is no background flow ($\mathbf{u}^\infty = 0$) then the integrals over S in (15) both vanish as the radius of S becomes infinite and we obtain

$$\begin{aligned} 0 &= \int_D \psi_j(\mathbf{y}) \left[c\mu (U_j + (\boldsymbol{\Omega} \times (\mathbf{x} - \mathbf{Y}))_j) - \frac{1}{2} f_j(\mathbf{y}) - \frac{1}{8\pi} n_k(\mathbf{y}) \int_D T_{ijk}(\mathbf{x}, \mathbf{y}) f_i(\mathbf{x}) dS_x \right. \\ &\quad \left. - \frac{c}{8\pi} \int_D C_{ij}(\mathbf{x}, \mathbf{y}) f_i(\mathbf{x}) dS_x \right] dS_y, \end{aligned} \quad (19)$$

which, because ψ is arbitrary, leads to the desired integral equation for \mathbf{f} . In our notation this is

$$\frac{1}{2} f_j(\mathbf{y}) + \frac{1}{8\pi} n_k(\mathbf{y}) \int_D T_{ijk}(\mathbf{x}, \mathbf{y}) f_i(\mathbf{x}) dS_x + \frac{c}{8\pi} \int_D C_{ij}(\mathbf{x}, \mathbf{y}) f_i(\mathbf{x}) dS_x = c\mu (U_j + (\boldsymbol{\Omega} \times (\mathbf{x} - \mathbf{Y}))_j), \quad (20)$$

and this holds for each $\mathbf{y} \in D$ and for each $j = 1, 2, 3$. This is equivalent to equation (20) in [78]. The previously published equation is identical despite our inclusion of a minus sign in the stresslet, as is more conventional; the sign change is effectively absorbed by the freedom of choosing the completion flow.

If there is in fact a background flow, then $\langle \mathbf{u}', \mathbf{f} \rangle_S$ and $\langle \mathbf{u}, \mathbf{f}' \rangle_S$ do not vanish as the radius of the bounding sphere S tends to infinity. We must therefore write these also in the form $\langle \psi, \cdot \rangle_D$. For the first we have

$$\begin{aligned} \langle \mathbf{u}', \mathbf{f} \rangle_S &= \langle \mathbf{u}', \mathbf{f}^\infty \rangle_S \\ &= \int_S f_i^\infty(\mathbf{x}) \int_D \psi_j(\mathbf{y}) \left[\frac{1}{8\pi} T_{ijk}(\mathbf{x}, \mathbf{y}) n_k(\mathbf{y}) + \frac{c}{8\pi} C_{ij}(\mathbf{x}, \mathbf{y}) \right] dS_y dS_x \\ &= \int_D \psi_j(\mathbf{y}) \int_S f_i^\infty(\mathbf{x}) \left[\frac{1}{8\pi} T_{ijk}(\mathbf{x}, \mathbf{y}) n_k(\mathbf{y}) + \frac{c}{8\pi} C_{ij}(\mathbf{x}, \mathbf{y}) \right] dS_x dS_y. \end{aligned} \quad (21)$$

The remaining integral involves the traction field \mathbf{f}' of the flow arising from ψ at the inner surface of the bounding sphere S , so the stress fields of the stresslet and of the completion flow are required. The tensor T_{ijk}^{STR} generating the stress field corresponding to the stresslet velocity field was given in Table I. Denote by

$C_{ijk}^{STR}(\mathbf{x}, \mathbf{y})$ the kernel for the stress field of the completion flow, which we leave general for the moment. Then we may proceed to write

$$\begin{aligned}
\langle \mathbf{u}, \mathbf{f}' \rangle_S &= \langle \mathbf{u}^\infty, \mathbf{f}' \rangle_S \\
&= \int_S u_i^\infty(\mathbf{x}) \sigma'_{im}(\mathbf{x}) \hat{n}_m(\mathbf{x}) dS_{\mathbf{x}} \\
&= \int_S u_i^\infty(\mathbf{x}) \hat{n}_m(\mathbf{x}) \int_D \psi_j(\mathbf{y}) \left[\frac{\mu}{8\pi} T_{ijk}^{STR}(\mathbf{x}, \mathbf{y}) n_k(\mathbf{y}) + \frac{c\mu}{8\pi} C_{ijm}^{STR}(\mathbf{x}, \mathbf{y}) \right] dS_{\mathbf{y}} dS_{\mathbf{x}} \\
&= \int_D \psi_j(\mathbf{y}) \int_S u_i^\infty(\mathbf{x}) \hat{n}_m(\mathbf{x}) \left[\frac{\mu}{8\pi} T_{ijk}^{STR}(\mathbf{x}, \mathbf{y}) n_k(\mathbf{y}) + \frac{c\mu}{8\pi} C_{ijm}^{STR}(\mathbf{x}, \mathbf{y}) \right] dS_{\mathbf{x}} dS_{\mathbf{y}},
\end{aligned} \tag{22}$$

where \hat{n} is an inward pointing normal vector on S .

Now all four terms in (15) have been rewritten as inner products against the arbitrary function ψ . Collecting these into a single inner product against ψ and recalling that ψ was arbitrary, we conclude that the other argument in the inner product must vanish identically.³ This leads to an integral equation for the unknown surface tractions \mathbf{f} on D ,

$$\begin{aligned}
\frac{1}{2} f_j(\mathbf{y}) + \frac{1}{8\pi} n_k(\mathbf{y}) \int_D T_{ijk}(\mathbf{y}', \mathbf{y}) f_i(\mathbf{y}') dS_{\mathbf{y}'} + \frac{c}{8\pi} \int_D C_{ij}(\mathbf{y}', \mathbf{y}) f_i(\mathbf{y}') dS_{\mathbf{y}'} \\
= c\mu(U_j + \epsilon_{jkl} \Omega_k (y_\ell - Y_\ell)) + \int_S u_i^\infty(\mathbf{x}) \hat{n}_m(\mathbf{x}) \left[\frac{\mu}{8\pi} T_{ijk}^{STR}(\mathbf{x}, \mathbf{y}) n_k(\mathbf{y}) + \frac{c\mu}{8\pi} C_{ijm}^{STR}(\mathbf{x}, \mathbf{y}) \right] dS_{\mathbf{x}} \\
- \int_S f_i^\infty(\mathbf{x}) \left[\frac{1}{8\pi} T_{ijk}(\mathbf{x}, \mathbf{y}) n_k(\mathbf{y}) + \frac{c}{8\pi} C_{ij}(\mathbf{x}, \mathbf{y}) \right] dS_{\mathbf{x}}, \tag{23}
\end{aligned}$$

which holds for $j = 1, 2, 3$ and for all $\mathbf{y} \in D$. Comparing this to (20) we see that the inclusion of a background flow has modified only the right-hand side of the integral equation, leaving unchanged the operator which must be inverted.

The integral equation (23) holds for any background flow which solves the unforced Stokes equations (2), and for any completion flow. To apply this equation for a specific background flow we must evaluate the integrals over the bounding sphere S , which can have any desired radius as long as it contains the particle. In principle this can be done numerically, but it is more convenient if the integrals over S converge to analytically tractable expressions in the limit of large radius. This occurs for a linear background flow, so we now take $u_i^\infty(\mathbf{x}) = A_{ij}x_j$ and $\sigma_{ik}^\infty(\mathbf{x}) = \mu(A_{ik} + A_{ki})$, where A has zero trace to satisfy incompressibility. At the same time we assume a completion flow with the kernel

$$C_{ij}(\mathbf{x}, \mathbf{y}) = G_{ij}(\mathbf{x}, \mathbf{z}(\mathbf{y})) + \epsilon_{m\ell j} R_{im}(\mathbf{x}, \mathbf{z}(\mathbf{y}))(y_\ell - z_\ell(\mathbf{y})), \tag{24}$$

where G_{ij} and R_{ij} are given in Table I and $\mathbf{z} : D \rightarrow \text{Int } D$ is a map from the surface to the interior of the particle; in the case that $\mathbf{z} \equiv \mathbf{Y}$ (a Stokeslet and rotlet are placed at the particle centroid) this is the completion flow of Power and Miranda [77]. The kernel for the stress field of this flow is

$$C_{ijk}^{STR}(\mathbf{x}, \mathbf{y}) = \mu G_{ijk}^{STR}(\mathbf{x} - \mathbf{z}(\mathbf{y})) + \mu \epsilon_{m\ell j} R_{imk}^{STR}(\mathbf{x}, \mathbf{z}(\mathbf{y}))(y_\ell - z_\ell(\mathbf{y})), \tag{25}$$

where G^{STR} and R^{STR} are given in Table I. The integrals on the right-hand side of (23) are evaluated in Appendix B, resulting in the final integral equation for tractions on a rigid body moving with velocity

³ More precisely, the Riesz lemma implies that if the inner product $\langle \mathcal{F}, \psi \rangle$ vanishes for all ψ in a dense subset of a Hilbert space, then in fact $\mathcal{F} = 0$. Our Hilbert space is $L^2(D)^3$ with inner product $\langle \mathbf{u}, \mathbf{v} \rangle = \int_D \mathbf{u} \cdot \mathbf{v} dS$ and the dense subset is the collection of smooth functions.

$\mathbf{U} + \boldsymbol{\Omega} \times (\mathbf{x} - \mathbf{Y})$ in an infinite fluid with background flow $\mathbf{u}^\infty(\mathbf{x}) = A\mathbf{x}$:

$$\begin{aligned} & \frac{1}{2}f_j(\mathbf{y}) + \frac{1}{8\pi}n_k(\mathbf{y}) \int_D T_{ijk}(\mathbf{y}', \mathbf{y})f_i(\mathbf{y}')dS_{\mathbf{y}'} + \frac{c}{8\pi} \int_D C_{ij}(\mathbf{y}', \mathbf{y})f_i(\mathbf{y}')dS_{\mathbf{y}'} \\ &= c\mu \left(U_j + \epsilon_{jkl}\Omega_k(Y_\ell - Y_\ell) \right) - \mu(A_{jk} + A_{kj})n_k(\mathbf{y}) + \frac{c\mu}{2}(A_{jk} - A_{kj})y_k + \frac{c\mu}{2}(A_{jk} + A_{kj})z_k(\mathbf{y}). \end{aligned} \quad (26)$$

Note that the identity (12) and the antisymmetry property $T_{ijk}(\mathbf{x}, \mathbf{y}) = -T_{ijk}(\mathbf{y}, \mathbf{x})$ of the free-space stresslet lead to a singularity subtraction which gives a version better suited for discretization:

$$\begin{aligned} & \frac{1}{8\pi} \int_D T_{ijk}(\mathbf{y}', \mathbf{y}) \left(f_i(\mathbf{y}')n_k(\mathbf{y}) + f_i(\mathbf{y})n_k(\mathbf{y}') \right) dS_{\mathbf{y}'} + \frac{c}{8\pi} \int_D C_{ij}(\mathbf{y}', \mathbf{y})f_i(\mathbf{y}')dS_{\mathbf{y}'} \\ &= c\mu \left(U_j + \epsilon_{jkl}\Omega_k(Y_\ell - Y_\ell) \right) - \mu(A_{jk} + A_{kj})n_k(\mathbf{y}) + \frac{c\mu}{2}(A_{jk} - A_{kj})y_k + \frac{c\mu}{2}(A_{jk} + A_{kj})z_k(\mathbf{y}). \end{aligned} \quad (27)$$

The subtracted singularity has the regularity of a bounded jump discontinuity [78].

B. Near a no-slip wall

A no-slip wall at $\{x_3 = 0\}$ can be accounted for with only a few modifications to the preceding argument. We begin by replacing the free-space stresslet $T_{ijk}(\mathbf{x}, \mathbf{y})$ in (16) with its half-space counterpart, $T_{ijk}^{\text{half}}(\mathbf{x}, \mathbf{y})$, which is derived using the Lorentz reflection procedure (see Appendix A) and given in Table III. The completion flow in (16) is subject to the additional requirement of vanishing on the wall, but is allowed to become singular below the wall. We then apply the reciprocal theorem on the volume external to the particle, above the wall, and below a large hemisphere H which is centered at $(Y_1, Y_2, 0)$. Both flows vanish on the wall, and if there is no background flow the integrals over H decay as the radius of H increases, yielding (20) but with the free-space singularities replaced by their wall-bounded counterparts; the integral equation is then

$$\frac{1}{2}f_j(\mathbf{y}) + \frac{1}{8\pi}n_k(\mathbf{y}) \int_D T_{ijk}^{\text{half}}(\mathbf{x}, \mathbf{y})f_i(\mathbf{x})dS_{\mathbf{x}} + \frac{c}{8\pi} \int_D C_{ij}^{\text{half}}(\mathbf{x}, \mathbf{y})f_i(\mathbf{x})dS_{\mathbf{x}} = c\mu \left(U_j + (\boldsymbol{\Omega} \times (\mathbf{x} - \mathbf{Y}))_j \right). \quad (28)$$

With a nonzero background flow the right-hand side includes integrals over H :

$$\begin{aligned} & \frac{1}{2}f_j(\mathbf{y}) + \frac{1}{8\pi}n_k(\mathbf{y}) \int_D T_{ijk}^{\text{half}}(\mathbf{x}, \mathbf{y})f_i(\mathbf{x})dS_{\mathbf{x}} + \frac{c}{8\pi} \int_D C_{ij}^{\text{half}}(\mathbf{x}, \mathbf{y})f_i(\mathbf{x})dS_{\mathbf{x}} \\ &= c\mu \left(U_j + (\boldsymbol{\Omega} \times (\mathbf{x} - \mathbf{Y}))_j \right) + \int_H u_i^\infty(\mathbf{x})\hat{n}_m(\mathbf{x}) \left[\frac{\mu}{8\pi} T_{ijkm}^{\text{half}, STR}(\mathbf{x} - \mathbf{y})n_k(\mathbf{y}) + \frac{c\mu}{8\pi} C_{ijm}^{\text{half}, STR}(\mathbf{x}, \mathbf{y}) \right] dS_{\mathbf{x}} \\ & \quad - \int_H f_i^\infty(\mathbf{x}) \left[\frac{1}{8\pi} T_{ijk}^{\text{half}}(\mathbf{x} - \mathbf{y})n_k(\mathbf{y}) + \frac{c}{8\pi} C_{ij}^{\text{half}}(\mathbf{x}, \mathbf{y}) \right] dS_{\mathbf{x}}. \end{aligned} \quad (29)$$

The only linear background flow satisfying a no-slip condition at $\{x_3 = 0\}$ is a shear flow. Without loss of generality we may suppose the direction of shear flow is parallel to the x -direction: $\mathbf{u}^\infty(\mathbf{x}) = \dot{\gamma}x_3\hat{\mathbf{x}}_1$. We specialize to this case and we assume a completion flow of the form

$$C_{ij}^{\text{half}}(\mathbf{x}, \mathbf{y}) = \frac{c}{8\pi} G_{ij}^{\text{half}}(\mathbf{x}, z(\mathbf{y})) + \frac{c}{8\pi} \epsilon_{m\ell j} R_{im}^{\text{half}}(\mathbf{x}, z(\mathbf{y}))(y_\ell - z_\ell(\mathbf{y})), \quad (30)$$

where the half-space Stokeslet and rotlet are given in Table III.

We then compute the integrals over H in the limit of large radius. Although the wall-bounded analogues of (B5) and (B7) converge to different expressions than in the free-space case, the differences are opposites

and so the sum of the four integrals is the same as above. The result is a completed traction integral equation for the rigid motion of a single particle above a no-slip wall in a background shear flow:

$$\begin{aligned} & \frac{1}{2}f_j(\mathbf{y}) + \frac{1}{8\pi}n_k(\mathbf{y}) \int_D T_{ijk}^{\text{half}}(\mathbf{y}', \mathbf{y}) f_i(\mathbf{y}') dS_{\mathbf{y}'} + \frac{c}{8\pi} \int_D C_{ij}^{\text{half}}(\mathbf{y}', \mathbf{y}) f_i(\mathbf{y}') dS_{\mathbf{y}'} \\ &= c\mu(U_j + \epsilon_{jkl}\Omega_k(y_\ell - Y_\ell)) - \mu\dot{\gamma}(\delta_{1j}n_3(\mathbf{y}) + \delta_{3j}n_1(\mathbf{y})) + \frac{c\mu\dot{\gamma}}{2}(\delta_{1j}y_3 - \delta_{3j}y_1) + \frac{c\mu\dot{\gamma}}{2}(\delta_{1j}z_3(\mathbf{y}) + \delta_{3j}z_1(\mathbf{y})). \end{aligned} \quad (31)$$

The right-hand side of this equation is identical to that of (26), once we specialize to $A_{jk} = \dot{\gamma}\delta_{1j}\delta_{3k}$.

We close with a comment on the singularity subtraction for the wall-bounded operator. The only term in the expression for $T_{ijk}^{\text{half}}(\mathbf{x}, \mathbf{y})$ in Table III which diverges as $\mathbf{x} \rightarrow \mathbf{y}$ is precisely the free-space stresslet, so we decompose the wall-bounded operator into bounded and diverging parts and then carry out the same subtraction as above for the diverging part. This leads to the subtraction

$$\begin{aligned} & \frac{1}{2}f_j(\mathbf{y}) + \frac{n_k(\mathbf{y})}{8\pi} \int_D T_{ijk}^{\text{half}}(\mathbf{y}', \mathbf{y}) f_i(\mathbf{y}') dS_{\mathbf{y}'} \\ &= \frac{1}{8\pi} \int_D [T_{ijk}(\mathbf{y}', \mathbf{y})(f_i(\mathbf{y}')n_k(\mathbf{y}) + f_i(\mathbf{y})n_k(\mathbf{y}')) + n_k(\mathbf{y})T_{ijk}^*(\mathbf{y}', \mathbf{y})f_i(\mathbf{y}')] dS_{\mathbf{y}'}, \end{aligned} \quad (32)$$

where $T^* = T^{\text{half}} - T$, the image singularity system of the free-space stresslet, is regular throughout the fluid domain. This subtraction should be applied to the equations (28) and (31) before discretization to reduce the singularity of the integrand to that of a bounded jump discontinuity.

IV. NUMERICAL METHOD AND VERIFICATION

A. Discrete equations

We now consider a simple collocation discretization of the equations derived in the previous section. In this scheme we encode all of the information about the particle geometry in a list of boundary points \mathbf{y}^p , normal vectors \mathbf{n}^p at those points, and quadrature weights w_p selected such that $\int_D \psi(\mathbf{x}) dS_{\mathbf{x}} \approx \sum_{p=1}^N \psi(\mathbf{y}^p) w_p$. In particular, two methods are used for generating the surface quadrature rules in this paper, one which takes advantage of axisymmetric geometries and the other applicable for particles of general shape. In the first method, we use a spherical coordinate system and represent particle points as $\mathbf{y}(\phi, \eta) = r(\phi)(\cos(\phi), \sin(\phi)\cos(\eta), \sin(\phi)\sin(\eta))$ where $r(\phi)$ is a specified profile. Gaussian quadrature is applied in the zenith angle ϕ and the trapezoidal rule with between 9 and 18 nodes is used in the azimuthal angle η . The second method is based on a triangular mesh of the body; in particular we use `distmesh` [88] to generate uniform triangular meshes, in which case the quadrature nodes are the mesh vertices, the vertex normals are the area weighted average of adjacent face normals, and the weights are simply one-third of the sum of areas of adjacent (flat) triangles.

With any quadrature $\{(\mathbf{y}^p, \mathbf{n}^p, w_p)\}_{p=1}^N$, the free-space integral operator at the source point $\mathbf{y} \in D$ is approximated by

$$\begin{aligned} & \frac{1}{8\pi} \int_D T_{ijk}(\mathbf{y}', \mathbf{y})(f_i(\mathbf{y}')n_k(\mathbf{y}) + f_i(\mathbf{y})n_k(\mathbf{y}')) dS_{\mathbf{y}'} + \frac{c}{8\pi} \int_D C_{ij}(\mathbf{y}', \mathbf{y}) f_i(\mathbf{y}') dS_{\mathbf{y}'} \\ & \approx \sum_{p=1}^N \left[\frac{1}{8\pi} T_{ijk}(\mathbf{y}^p, \mathbf{y})(f_i(\mathbf{y}^p)n_k(\mathbf{y}) + f_i(\mathbf{y})n_k(\mathbf{y}^p)) + \frac{c}{8\pi} C_{ij}(\mathbf{y}^p, \mathbf{y}) f_i(\mathbf{y}^p) \right] w_p. \end{aligned} \quad (33)$$

The integral equation is required to hold at the quadrature nodes $\mathbf{y} = \mathbf{y}^q$, for $q = 1, \dots, N$. The stresslet term

(with singularity subtraction) in the integrand of (33) has a bounded jump discontinuity at the source point \mathbf{y} for a smooth surface; fortunately, in simply omitting the source point from the sum, both quadrature schemes above retain second-order accuracy (see [77, 78], and note that the local form of the jump singularity averages to zero upon integration over a small circular patch.) That is, we determine the $3N$ unknowns $f_j(\mathbf{y}^q)$ which solve the $3N$ equations

$$\begin{aligned} & \sum_{p \neq q} \frac{1}{8\pi} T_{ijk}(\mathbf{y}^p, \mathbf{y}^q) (f_i(\mathbf{y}^p) n_k(\mathbf{y}^q) + f_i(\mathbf{y}^q) n_k(\mathbf{y}^p)) w_p + \frac{c}{8\pi} \sum_{p=1}^N C_{ij}(\mathbf{y}^p, \mathbf{y}^q) f_i(\mathbf{y}^p) w_p \\ & = c\mu \left(U_j + \epsilon_{jkl} \Omega_k (y_\ell^q - Y_\ell) \right) - \mu (A_{jk} + A_{kj}) n_k(\mathbf{y}^q) + \frac{c\mu}{2} (A_{jk} - A_{kj}) y_k^q + \frac{c\mu}{2} (A_{jk} + A_{kj}) z_k(\mathbf{y}^q), \end{aligned} \quad (34)$$

for $j = 1, 2, 3$ and $q = 1, \dots, N$. With a wall, the discrete equations are instead

$$\begin{aligned} & \sum_{p \neq q} \frac{1}{8\pi} T_{ijk}(\mathbf{y}^p, \mathbf{y}^q) (f_i(\mathbf{y}^p) n_k(\mathbf{y}^q) + f_i(\mathbf{y}^q) n_k(\mathbf{y}^p)) w_p \\ & + \frac{1}{8\pi} n_k(\mathbf{y}^q) \sum_{p=1}^N T_{ijk}^*(\mathbf{y}^p, \mathbf{y}^q) f_i(\mathbf{y}^p) w_p + \frac{c}{8\pi} \sum_{p=1}^N C_{ij}^{\text{half}}(\mathbf{y}^p, \mathbf{y}^q) f_i(\mathbf{y}^p) w_p \\ & = c\mu \left(U_j + \epsilon_{jkl} \Omega_k (y_\ell^q - Y_\ell) \right) - \mu \dot{\gamma} (\delta_{1j} n_3(\mathbf{y}^q) + \delta_{3j} n_1(\mathbf{y}^q)) + \frac{c\mu \dot{\gamma}}{2} (\delta_{1j} y_3^q - \delta_{3j} y_1^q) + \frac{c\mu \dot{\gamma}}{2} (\delta_{1j} z_3(\mathbf{y}^q) + \delta_{3j} z_1(\mathbf{y}^q)). \end{aligned} \quad (35)$$

In all cases to be described we adopt the Power and Miranda completion flow, setting $\mathbf{z}(\mathbf{y}) \equiv \mathbf{Y}$ with \mathbf{Y} the particle centroid. The discrete linear system of equations is dense and non-normal. We solve it using the generalized minimal residual algorithm (GMRES) [89] without preconditioning or restarting until a relative residual of 10^{-12} is reached.

B. Mobility formulation

So far, we have discussed the resistance problem where the particle velocity is prescribed and the surface tractions as well as the net force and torque are unknown. Solving instead the mobility problem, where the net force and torque are imposed and the surface tractions and the rigid-body velocity are unknown, requires only a minor modification to (34) (or (35)). The terms involving the six constants U_j and Ω_k are subtracted from the right-hand to the left-hand side and these become additional unknowns, and the system is closed by enforcing

$$\sum_{p=1}^N f_j(\mathbf{y}^p) w_p = F_j, \quad \sum_{p=1}^N \epsilon_{jkl} (y_k^p - Y_k) f_\ell(\mathbf{y}^p) w_p = L_j, \quad (36)$$

for $j = 1, 2, 3$ (recall that \mathbf{F} and \mathbf{L} denote the imposed net force and torque exerted by the fluid on the particle).

C. Validation

To demonstrate the accuracy of the free-space discrete system (34), we consider the case of a rigid sphere held fixed in a background shear flow with a unit shear rate: $|\mathbf{u}(\mathbf{x}) - x_3 \hat{\mathbf{x}}_1| \rightarrow 0$ as $|\mathbf{x}| \rightarrow \infty$ and $\mathbf{u}(\mathbf{x}) = \mathbf{0}$ for $|\mathbf{x}| = a$, for which an exact solution is known [79]. The analytical disturbance velocity field may be written as the sum of a rotlet, a stresslet, and the Laplacian of a stresslet placed at the center of the sphere,

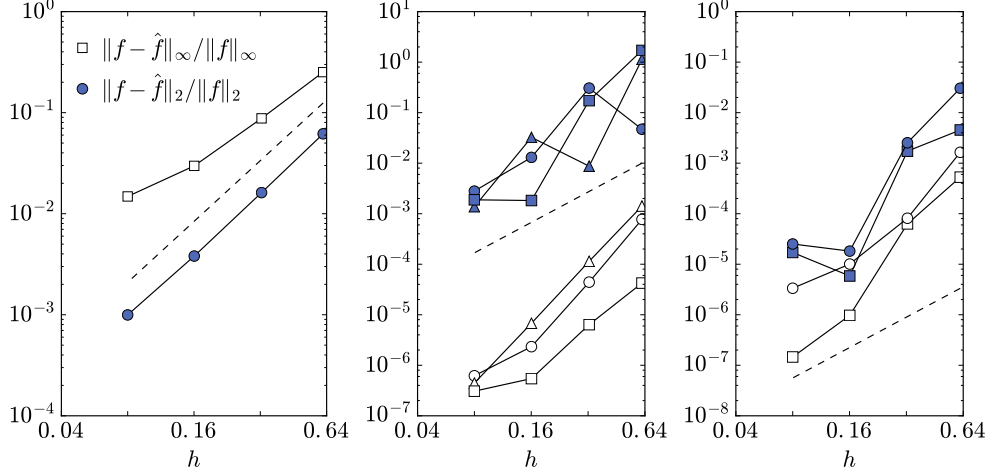


FIG. 1. Validation of the numerical method. Left panel: L^2 and L^∞ errors in the computed surface traction field on a sphere held immobile in a background shear flow versus maximum triangle edge length h on a logarithmic scale. Center panel: absolute error in the net force (circles) and torque (squares) on a sphere translating parallel to the wall, and torque (triangles) on a sphere rotating with rotation axis parallel to the wall. The distance of the centroid to the wall is $H = \cosh(2)$ (far from the wall; open symbols) or $H = \cosh(0.3)$ (near the wall; filled symbols). Right panel: absolute error in the force (squares) and torque (circles) on a sphere held fixed in a background shear flow. Open/filled symbols indicate the same distances to the wall as in the center panel. Dashed lines scale as h^2 for reference, indicating second-order accuracy of the numerical method.

resulting in

$$\begin{aligned}
 u_i(\mathbf{x}) &= \delta_{1i}x_3 - \frac{a^3}{2} \frac{\epsilon_{ijk}x_k}{r^3} \delta_{2j} - \left(\frac{5a^3}{4} + \frac{a^5}{8} \nabla^2 \right) \frac{x_i x_j x_k}{r^5} s_{jk} \\
 &= \left(\frac{1}{2} - \frac{a^3}{2r^3} \right) \epsilon_{i2k} x_k + \left(\frac{1}{2} - \frac{a^5}{2r^5} \right) s_{ij} x_j + \left(\frac{5a^5}{4r^7} - \frac{5a^3}{4r^5} \right) x_i x_j x_k s_{jk},
 \end{aligned} \tag{37}$$

where $s_{jk} = \delta_{3j}\delta_{1k} + \delta_{1j}\delta_{3k}$. The corresponding pressure is given by

$$p(\mathbf{x}) = 0 - \mu \left(\frac{5a^3}{4} + \frac{a^5}{8} \nabla^2 \right) \left(-2 \frac{\delta_{jk}}{3r^3} + 2 \frac{x_j x_k}{r^5} \right) s_{jk} = \frac{-5\mu a^3}{2r^5} x_j x_k s_{jk}, \tag{38}$$

and the tractions at the sphere surface are given by

$$f_i(\mathbf{x}) = \left(-p(\mathbf{x})\delta_{im} + \mu \frac{\partial u_i}{\partial x_m} + \mu \frac{\partial u_m}{\partial x_i} \right) \frac{x_m}{a} = \frac{3\mu}{2a} \epsilon_{i2k} x_k + \frac{5\mu}{2a} s_{ij} x_j = \frac{\mu}{a} (4\delta_{1i}x_3 + \delta_{3i}x_1). \tag{39}$$

Although the body in this test is spherical, we wish to illustrate the accuracy of the method in a more general setting and so we will not exploit the symmetry in the problem, using instead a quadrature obtained from a triangulated mesh as described above. The first panel of Fig. 1 shows the relative L^2 and L^∞ errors between the exact traction field (39), with $\mu = 1$ and $a = 1$, and the computed results \hat{f} , obtained from (34), plotted on a logarithmic scale against the maximum mesh triangle edge length h . The decrease in the L^2 error is proportional to h^2 as expected (a dashed line with slope 2 is included for reference). The L^∞ error is also decreasing at nearly the same rate, but lags somewhat behind the L^2 accuracy. This may be

$H \setminus N$	54	198	828	3318
cosh(2)	24	23	22	20
cosh(0.3)	53	63	64	52

TABLE II. Number of GMRES iterations (without preconditioning or restarting) for the discrete resistance problems whose convergence to exact solutions appears on the right side of Figure 1. We solved three resistance problems at each of the indicated centroid-wall distances H and mesh vertex counts N , all three using the same matrix but different right-hand sides. The displayed iteration counts are for the translation problem; the counts for the other right-hand sides differ by no more than two. The iteration count decreases slightly when the grid is refined but increases with decreasing gap size.

a consequence of the coarser meshes not being subsets of the finer meshes; with a quadrature exploiting axisymmetry we observe a more obvious connection between the L^2 and L^∞ convergence rates (in fact we observed third-order accuracy when using a symmetric mesh in this test).

As a second test of the code we consider a wall-bounded problem (35), and compare the numerical results with exact solutions for the net force and torque on a unit sphere in a viscous fluid near a plane wall [90–92]. We consider several resistance problems and for each problem we compute solutions using several meshes, with the number of nodes ranging from $54 \leq N \leq 3318$, and at two values of the height of the sphere center above the wall, H . The absolute error in the net force (circles) and torque (squares) on a sphere translating parallel to the wall, and torque (triangles) on a sphere rotating with rotation axis parallel to the wall are shown in the center panel of Fig. 1. The distance of the centroid to the wall is $H = \cosh(2)$ (far from the wall; open symbols) and $H = \cosh(0.3)$ (close to the wall; filled symbols). Again a dashed line is included which scales as h^2 for reference, indicating second-order accuracy. The right panel of Fig. 1 shows the absolute error in the force (squares) and torque (circles) on a sphere held fixed in a background shear flow, with open and filled symbols indicating the same distances to the wall as in the center panel. In all of the cases studied the errors decrease as the square of the mesh diameter h as expected, and the error naturally depends strongly on the gap size between the particle and the wall. The number of GMRES iterations required to achieve relative residuals of 10^{-12} is modest compared to the system size, and in particular decreases as the discretization is refined. On the other hand, we found that it increases when the particle is close to a plane wall. See Table II for details.

V. APPLICATIONS

A. The role of particle eccentricity in sedimentation near a wall

The trajectory of a rigid spheroid sedimenting under the influence of gravity near a plane wall depends strongly on the eccentricity of the particle. In a previous study we used far-field approximations to produce analytical solutions for the body trajectory [93]. Several trajectory types are possible depending on the body shape and initial position and orientation, including glancing, reversing, and periodic tumbling. A surprising result from that study was the finding that a spherical body, which “rolls” down along a wall, is a very special case. Indeed, while nearly spherical bodies periodically wobble towards and away from the wall with a similar rolling-type rotation, a more eccentric prolate body with symmetry axis parallel to the wall can instead rotate in the opposite direction; see Fig. 2. More concretely, the far-field theory predicts this opposite rotation direction for a prolate body if the height H of its centroid above the wall satisfies $H^2 > (2 + e^2)/(3e^2)$ where e is the particle eccentricity [93]; such a body subsequently escapes from the wall and recedes into the bulk fluid never to return. Generally, escaping trajectories are classified as either glancing or reversing (see Fig. 3) depending on whether the particle is parallel or perpendicular to the wall at the moment of nearest approach. Which trajectory is selected depends on the particle aspect ratio, and

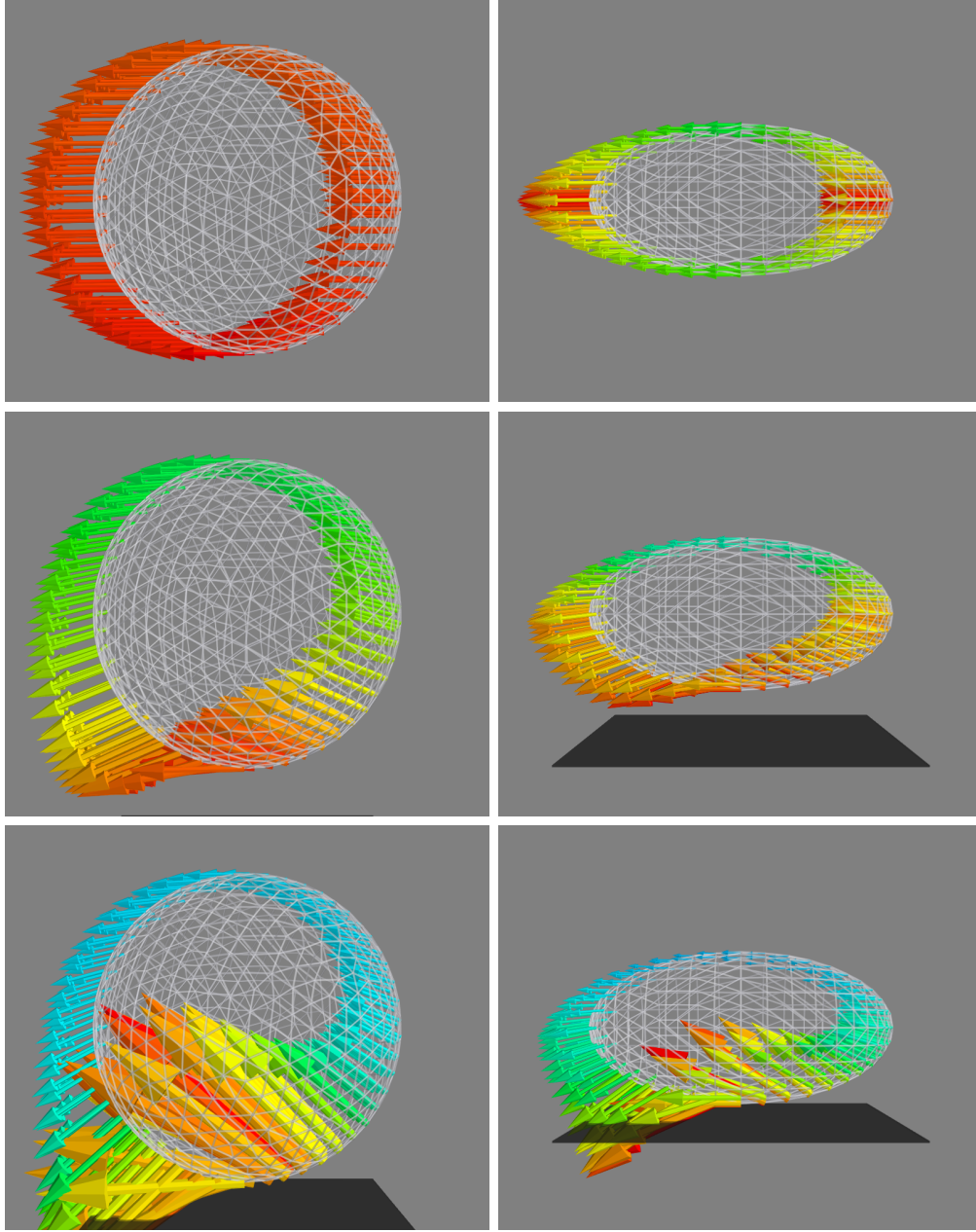


FIG. 2. Traction fields exerted by the fluid on torque-free particles moving under a unit force to the right (parallel to the wall) at three different distances to the wall. The wall is infinite in extent but represented visually by a finite square. Traction fields are plotted only at points near the $\{x_2 = 0\}$ plane for clarity. The traction fields are nearly up-down symmetric for particles far from the wall, but symmetry is broken strongly by a nearby wall. The resulting up-down asymmetry in the x_1 -component of traction induces a clockwise rotation on a torque-free body, whereas the front-back antisymmetry in the x_3 -component induces the opposite rotation. The net rotation due to the combination of these two effects is clockwise for the case of a sphere and counterclockwise for the prolate body, a distinction which accounts for the diverging trajectories of the two body shapes as previously studied [93].

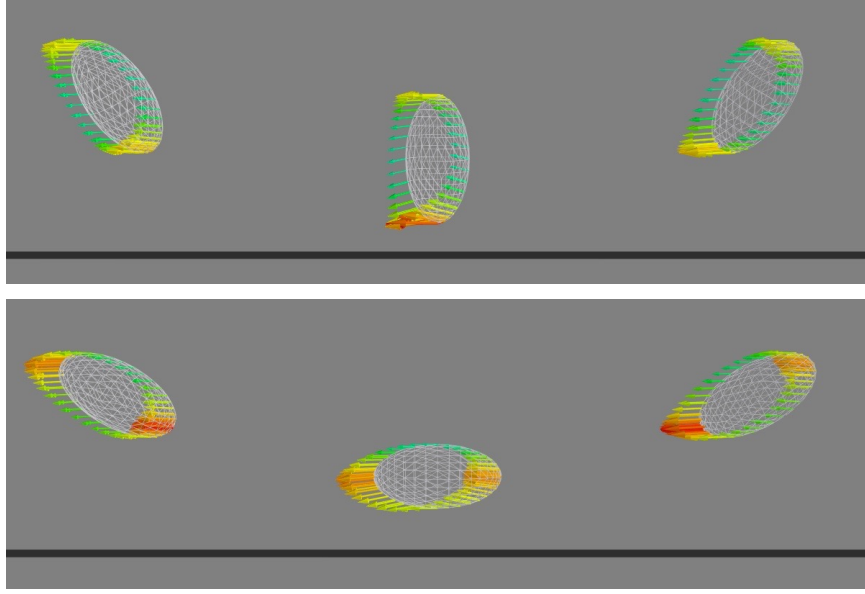


FIG. 3. Top: a prolate ellipsoid moves above a no-slip wall with a constant force to the right. Hydrodynamic traction vectors are shown with color and length both in proportion to magnitude. Stresses are largest when the nose of the body is closest to the wall, resulting in an overturning, or reversing orbit. Bottom: The same body, with a smaller initial angle between its major axis and the wall, undergoes instead a glancing orbit. When the body is closest to the wall, the tractions near the lowest point on the body are still larger than those on the highest part, which would lead to a reversing rotation, but there is a slight antisymmetry in the x_3 -component of the traction at the poles that instead results in an oppositely signed rotation.

the initial orientation angle and height of the body relative to the wall.

We now return to this problem to take a more detailed view of the local hydrodynamic stresses which lead to body rotation near a wall. We place a wall at $\{x_3 = 0\}$ and solve the mobility problem, imposing a unit force in the x_1 -direction on a rigid spherical particle or on a prolate spheroidal particle whose symmetry axis is aligned with the x_1 -direction. Figure 2 shows the computed tractions on these bodies at three different distances from the wall. For clarity, only the traction vectors at points near the $\{x_2 = 0\}$ plane are shown. When the particle is infinitely far from the wall, it is known that the traction on a sphere is uniform, and the traction on a spheroid has a simple representation in terms of the surface normal [94]; in particular the traction fields on both bodies at a large but finite distance from the wall are nearly symmetric vertically and horizontally. Both symmetries break down at smaller particle-wall gap sizes, and they break in such a way as to introduce opposing torques, which in turn promote opposing rotations since the particle is torque-free. The up-down asymmetry in the x_1 -component of the traction field corresponds to clockwise rotation, whereas the front-back antisymmetry in the x_3 -component corresponds to counterclockwise rotation. For the sphere, the up-down asymmetry is more powerful and the particle rotates in the clockwise direction. The situation is reversed for the prolate body: the front-back antisymmetry dominates because the locations of the strongest x_3 -tractions are better separated than in the spherical case, resulting in a longer moment arm. A similar competition between of viscous stresses is observed throughout the typical glancing and reversing trajectories shown in Fig. 3.

B. Viscous erosion

As a second application we study the erosion of a body which is held immobile in a uniform flow $\mathbf{u}^\infty(\mathbf{x}) = U\hat{\mathbf{x}}_1$ or in a shear flow $\mathbf{u}^\infty(\mathbf{x}) = \dot{\gamma}x_3\hat{\mathbf{x}}_1$. The surface is assumed to recede at a rate proportional to the local shear stress,

$$\dot{\mathbf{x}} = -\alpha |(\mathbf{I} - \mathbf{n}\mathbf{n}) \cdot \mathbf{f}| \mathbf{n}, \quad (40)$$

where \mathbf{f} is the surface traction and α is a proportionality constant. This ablation model was found to accurately describe the erosion of a clay cylinder in an inertial flow [50]. Assuming that the rate of particle erosion is small when compared to the background flow, the shape dynamics may be studied by a quasi-steady approximation. In other words, the no-slip velocity boundary condition is applied on a rigid moving body to determine the traction, which is used in (40).

We begin by simulating the erosion of an initially spherical body held fixed in a uniform background flow in an infinite fluid. The problem is made dimensionless by scaling lengths on the initial body radius a_0 , velocities on the background flow speed U , forces on $\mu U a_0$, and time on a characteristic erosion timescale $t_v = a_0^2/(\alpha \mu U)$. Henceforth all variables are assumed to be dimensionless. By symmetry considerations the particle must remain axisymmetric throughout the erosion process, and unlike in an inertial flow it must also retain a fore-aft symmetry (seen by taking $x_1 \rightarrow -x_1$ and $u_1(\mathbf{x}) \rightarrow -u_1(\mathbf{x})$ in (1). The surface of the body at time t is therefore parameterized in a spherical coordinate system as described in §IV with a radius function $r(\phi) \in C[0, \pi/2]$, extended symmetrically for $\phi \in [\pi/2, \pi]$ by $r(\phi) = r(\pi/2 - \phi)$. The function $r(\phi)$ is represented numerically as a piecewise cubic spline on $[0, \pi/2]$ with 37 equally spaced internal knots; the quadrature rule for the body surface is then generated using 150 Gauss quadrature nodes on $[0, \pi]$ and 18-point trapezoidal integration in the azimuthal direction. The surface tractions are computed from (34) and the particle shape is updated using (40), with timesteps chosen adaptively so that unit normal vectors change by less than 0.001 in the L^2 norm per step. After each timestep, all of the points on the body surface are used to generate a new spline function representing the updated profile $r(\phi)$.

The top row of Fig. 4 shows the shape of the eroding particle at three different times, with regions of increased shear stress indicated by a darker color. As soon as the erosion begins the body loses its smoothness at the leading and trailing stagnation points, $\mathbf{x} = (\pm 1, 0, 0)$, instantly taking a locally conical geometry there. Cross-sectional profiles of the body at equally spaced moments in time are shown in the second row of Fig. 4, in unscaled coordinates and then scaled by the semiaxis length in the direction of flow, $\ell(t)$, to align the horizontal axis lengths at all times. The first set of profiles illustrate the accelerating reduction of length and width as the body becomes smaller and as the aspect ratio decreases. The profiles are again colored according to the magnitude of shear stress, and we note in particular the gradual shift of the maximal shear stress from the body midsection towards the conical endpoints. The shift of the maximal shear stress from the midsection towards the nose and tip is demonstrated more directly on the left in Fig. 5, showing an initial profile which is sinusoidal in the zenith angle ϕ , which then becomes more evenly distributed for intermediate times, and then finally inverting so that the regions of largest shear stress are in fact near the conical tips. The rescaled profiles in Fig. 4 demonstrate that the aspect ratio of the particle decreases monotonically throughout the evolution, a result which lies in contrast to the inertial study [50] where the rescaled geometry converged to a wedge-shaped region and then shrank in a self-similar fashion.

The half-length of the body, $\ell(t)$, and the half-thickness, $b(t)$, are plotted as symbols on the bottom row of Fig. 4. For small times $b(t)$ recedes at a much faster rate than $\ell(t)$, but as the leading and trailing ends become sharper the length reduction accelerates. Next the aspect ratio $b(t)/\ell(t)$ is shown, indicating a steady monotonic decrease over time with a very slight inflection at approximately $t = 0.2$, along with the surface area $A(t)$, which shows a nearly linear decrease until the particle vanishes. By the end of the simulation (which we halted once $A(t)/A(0) < 0.003$) the body reaches an aspect ratio of approximately 0.3. The

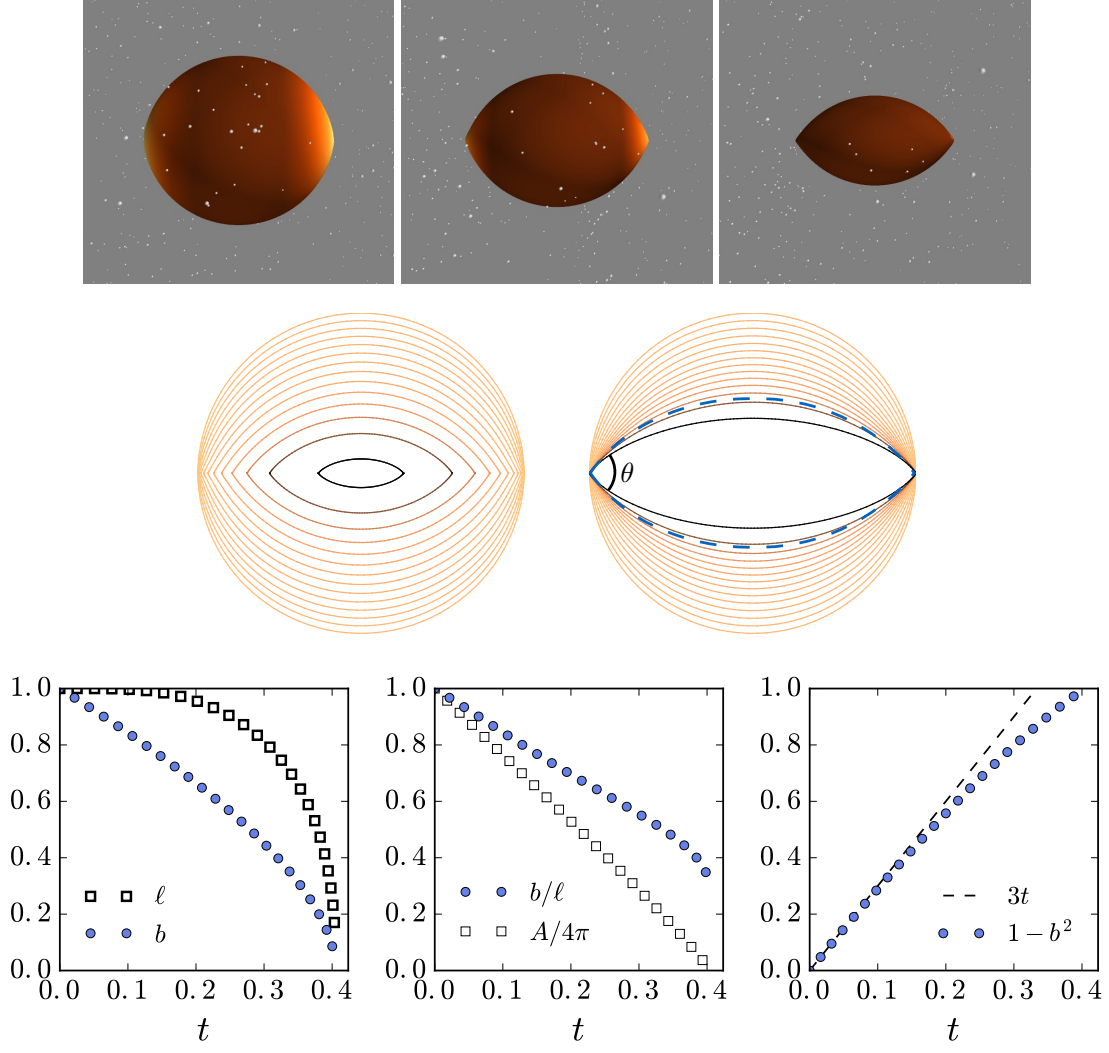


FIG. 4. Erosion of an initially spherical particle at low Reynolds number in a uniform horizontal background flow. Top row: the eroding particle at three equally spaced times, with shear stress colored by shear stress magnitude (darker color indicates a larger shear stress). Second row: cross-sectional profiles taken through the $\{x_2 = 0\}$ plane at equally spaced times (left) and scaled by the body half-length $\ell(t)$. The dashed line is Pironneau's drag-minimizing profile [95, 96], which is not the limiting body shape. Bottom row: The half-length $\ell(t)$ and half-thickness $b(t)$ as a function of dimensionless time (left), with comparison to theoretical prediction (center), and a time-series of the body aspect ratio and surface area $A(t)$.

simulations hint at a complete loss of volume in finite time, and we do not expect the aspect ratio to reduce much further before the body volume has vanished. Extrapolating from $A(t)$ we predict a finite vanishing time of $t_f \approx 0.41$. The opening angle θ is plotted as function of time on the right in Fig. 5, where we observe a steady initial decrease from the initial value of π to a value just below $3\pi/4$ before entering a period of much slower decay. The opening angle does not settle to a fixed value in the time of simulation, continuing to decrease very slowly, and reaching a value of $\theta = 0.67\pi$ by the end of the simulation. While the curves showing the aspect ratio b/ℓ in Fig. 4 and $\theta(t)$ in Fig. 5 suggest the possibility of a rapid change before the body vanishes, a more refined study of this late stage indicated no such effect.

Many aspects of the evolution observed in the numerical simulation just described can be understood better by analytical approximations. The early loss of regularity is a consequence of the uniform dimen-

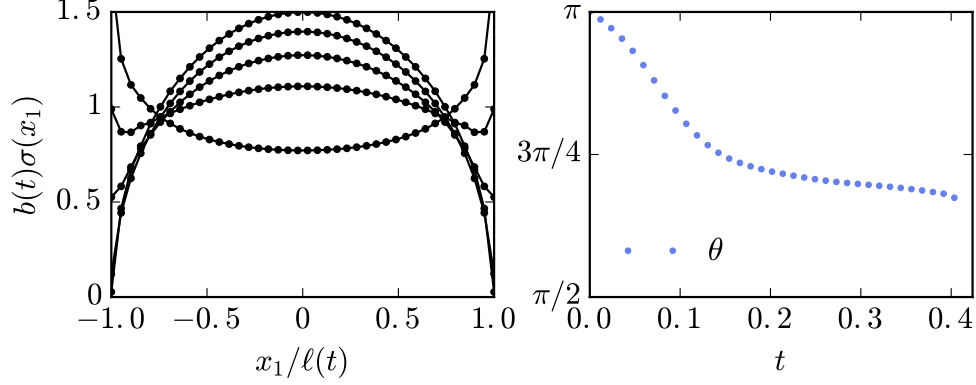


FIG. 5. Left: the thickness-scaled surface traction magnitude, $b(t)\sigma(x)$, with $\sigma = |(\mathbf{I} - \mathbf{n}\mathbf{n}) \cdot \mathbf{f}|$, at five equally-spaced moments from $t = 0$ to $t = 0.4$ as a function of length-scaled horizontal position $x_1/\ell(t)$, for the same simulation. Right: the opening angle θ for the eroding body in uniform flow depicted in figure 4, plotted against dimensionless time.

sionless traction $\mathbf{f} = (3/2)\hat{\mathbf{x}}_1$ as seen in the top left panel of Fig. 2. Indeed, the shear stress has magnitude $\sigma(\phi) = |(\mathbf{I} - \mathbf{n}\mathbf{n}) \cdot \mathbf{f}| = 3 \sin(\phi)/2$ (consistent with the shear stress plot at $t = 0$ in Fig. 5), so that by (40) the smooth surface develops a conical tip at $\phi = 0$ via $\dot{\mathbf{x}} \approx -3\phi/2(\hat{\mathbf{x}}_1 + \hat{\mathbf{r}}(\eta))$ with η the azimuthal angle. The opening angle is then given by $\theta(t) \sim \pi(1 - \sqrt{2}t)$ for very small t .

Meanwhile, the erosion rate along the equator at the midsection of the unit sphere is given by $\sigma(\pi/2) = 3/2$. Consider the approximation that this erosion rate applies uniformly on the body surface. Then the particle remains spherical at all times with dimensionless radius $a(t)$ (with $a(0) = 1$), and the dimensionless traction is given more generally by $\mathbf{f} = -3/(2a(t))\hat{\mathbf{x}}_1$. The radius would then decay as $a' = -3/(2a)$, so that $a(t) = \sqrt{1 - 3t}$. This approximation indicates a finite time of complete material loss, namely at a dimensionless time $t_f = 1/3$, a smaller vanishing time than is observed in the simulations, but which is quite a good estimate given the simplicity of the assumption. If instead we consider the decay of the midsection alone, we might assume for small times that the body length $\ell(t)$ remains roughly constant but the thickness $b(t)$ decays according to the calculation above, $b(t) = \sqrt{1 - 3t}$ or $1 - b(t)^2 = 3t$. This approximation is plotted in the rightmost panel of the bottom row of Fig. 4 as a dashed line, showing a close agreement with the simulations over a significant length of dimensionless time. The nearly linear decrease in the surface area $A(t)$ on the bottom right of Fig. 4 is also consistent with this scaling. The predicted power law scaling in the size, proportional to $(t_f - t)^{1/2}$ for $|t - t_f| \ll 1$, sits in contrast to the power law scaling observed at high Reynolds number, $(t_f - t)^{4/3}$ [51], though a more detailed mathematical investigation of the vanishing regime is still needed.

It would seem plausible that the shape of the eroding sphere should trend towards a limiting, self-similar profile as was found for the eroding body in an inertial flow [50], wherein the shear stress is uniform so that the shape is maintained while the volume shrinks. In particular, the drag-minimizing profile of a body with fixed volume in a uniform Stokes flow was shown by Pironneau to be that which everywhere has a constant vorticity (and hence shear stress) [95], resulting in a body with aspect ratio of approximately 0.477 : 1 and conical endpoints with an opening angle of $2\pi/3 = 120^\circ$ [96]. This profile is included for reference as a dashed line in Fig. 4. Why doesn't the body maintain this shape as it vanishes? To answer this we now show that the only profiles preserved under a constant erosion in the normal direction are those of a sphere and a cone.

Parameterizing the surface of an axisymmetric body as above by a function $r(\phi)$ describing the distance from the particle center as a function of the polar angle, we note that the condition $\dot{r}(\phi) \propto r(\phi)$ describes self-similar evolution. If the shear stress is given by $\alpha\chi(\phi)$, then (40) becomes $\dot{\mathbf{x}}(\phi) = -\alpha\chi(\phi)\mathbf{n}(\phi)$ and we

find the following condition for self-similar decay:

$$-\chi(\phi) \sqrt{1 + (r'(\phi)/r(\phi))^2} = \beta r(\phi),$$

where the decay parameter α has been folded into the constant of proportionality β . Equivalently, a profile $r(\phi)$ which recedes in the normal direction at a rate proportional to $\chi(\phi)$ remains self-similar if and only if

$$\frac{d}{d\phi} \left(-\chi(\phi) \sqrt{r(\phi)^{-2} + r'(\phi)^2 r(\phi)^{-4}} \right) = 0,$$

or

$$\chi'(\phi) r(\phi) (r(\phi)^2 + r'(\phi)^2) = \chi(\phi) r'(\phi) (r(\phi)^2 - r'(\phi) r(\phi) + 2r'(\phi)^2). \quad (41)$$

If the erosion rate is constant over the whole body, as it is for the drag-minimizing shape of Pironneau, then $\chi'(\phi)$ vanishes and we have

$$0 = r'(\phi) \left[-r(\phi)^2 - 2r'(\phi)^2 + r(\phi)r''(\phi) \right]. \quad (42)$$

The profile corresponding to $r'(\phi) = 0$ is the sphere and the other factor leads to the second-order ODE

$$0 = -r(\phi)^2 - 2r'(\phi)^2 + r(\phi)r''(\phi),$$

which has a two-parameter family of solutions given by $r(\phi) = c_1 c_2 [c_2 \cos(\phi) + c_1 \sin(\phi)]^{-1}$, which is the equation in polar coordinates of a straight line with intercepts $(0, c_2)$ and $(c_1, 0)$. This shows that if there is a limiting profile under erosion induced by uniform background flow then that limiting profile does not have constant shear stress, and in particular, that the profile of Pironneau cannot be the limiting shape of a particle eroding under the ablation law (40). Generally, a uniform interface velocity on a body with variable curvature does not result in a self-similar shape reduction, a point which was also made in the context of erosion at high Reynolds numbers [51].

The question remains whether there is a limiting profile of smaller aspect ratio than those achieved by the initially spherical particle in the time before dissolution. We also simulated the erosion of initially prolate bodies in a uniform background flow, but found that the aspect ratio always decreases monotonically even when the initial ratio is as small as 1:5. On this basis we conjecture that no profile eroding in a uniform flow according to (40) can shrink in a self-similar fashion.

1. Erosion in background shear flows and near surfaces

We now turn to the case of an immobile and initially spherical particle eroding under the influence of a background shear flow. Three configurations are considered: when the initial particle center lies in the plane of zero background flow in an infinite fluid, when it lies 1.5 radii above the plane of zero background flow, and finally when it lies 1.5 radii above a no-slip planar boundary. For the geometry discretization we begin with a uniform triangulation from `distmesh` which we then evolve without retriangulation according to (40). At each step, the normal vectors and quadrature weights are recomputed as described in §IV. Nondimensionalization is similar to that applied in the uniform flow, but scaling velocities instead upon $\dot{\gamma}$, the shear rate.

In the first problem the particle is placed at the origin and we let $\mathbf{u}^\infty(\mathbf{x}) = x_3 \hat{\mathbf{x}}_1$. The center of the particle then lies in the plane of zero background flow, resulting in top-down symmetry in addition to the ever-present fore-aft symmetry. Axisymmetry, however, is now broken by the background flow. The resulting evolution is depicted in the first row of Fig. 6 and a series of cross sections viewed along the

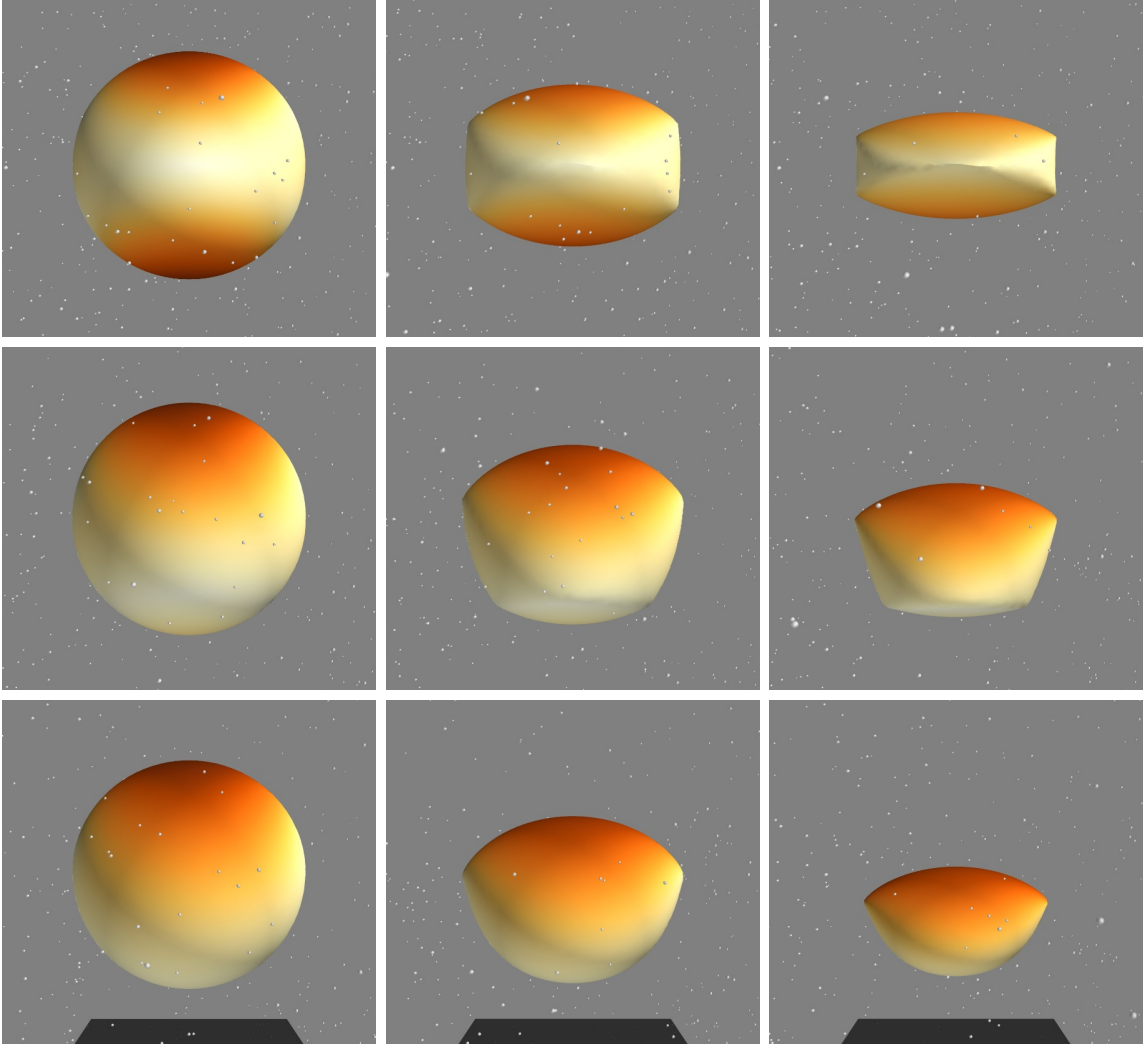


FIG. 6. Erosion of initially spherical particles at low Reynolds number while held immobile in a background shear flow. Top row: the fluid is infinite and the plane of zero shear flow meets the particle center. Second row: the fluid is infinite and the plane of zero shear lies 1.5 radii below the initial particle center. Bottom row: the fluid is bounded by a no-slip wall 1.5 radii below the initial particle center.

x_1 - and x_2 -directions are provided in Fig. 7 (a). Here again darker colors indicate locations of increased shear stresses. The surface regions facing the direction of flow experience relatively small viscous stresses at early times and the particle flattens due to the larger stresses near the extremal points in the direction of shear. In fact there is a recirculation region near the front and back of the particle relative to the flow direction resulting in a non-convex profile there. This slowly eroding non-convex region meets the more rapidly eroding regions on the top and bottom in a pair of corners, best viewed from the x_2 -direction in the top image of Fig. 7 (a). Meanwhile, along the neutral axis, the surface points with extremal x_2 -values develop into cusps, as can be seen in the profiles viewed from the x_1 -direction in Fig. 7. In the later stages of the evolution there are six corners, four in the $\{x_2 = 0\}$ plane and two in the $\{x_1 = 0\}$ plane.

Contours of the exact shear stress on the initially spherical body, along with streamlines of the exact fluid velocity at $t = 0$ (see (37)) are shown in Fig. 8a. This initial flow field has regions of recirculation between the stagnation points $(\pm 2/\sqrt{5}, 0, \pm 1/\sqrt{5})$, obtained from setting the tangential component of the traction field (39) to zero. This offers another perspective on why the surface recedes both in the recirculation

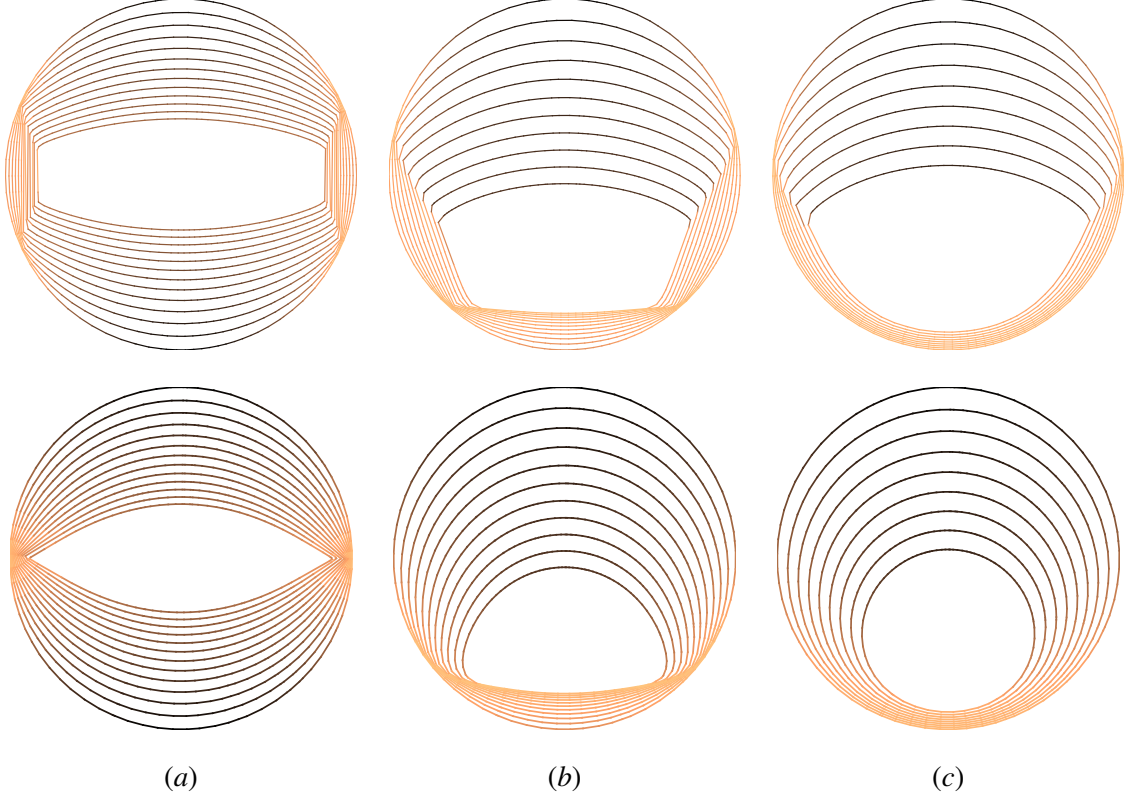


FIG. 7. Cross-sectional profiles of eroding bodies in a background shear flow corresponding to those shown in Fig. 6, equally spaced in time. The background flow is in the x_1 -direction and varies linearly in the x_3 -direction; the x_2 -direction is neutral. Shown are views from the neutral direction (top) and along the flow direction (bottom) for a body (a) centered in the plane of zero shear flow in an unbounded fluid; (b) set a distance 1.5 radii above the plane of zero shear flow in an unbounded fluid; and (c) a particle a distance 1.5 radii above a no-slip wall. Darker color indicates higher shear stress; the color scaling changes across rows but not within columns. Counting all of the sharp corners in each column, we find six, four, and two for (a), (b), and (c), respectively.

region and, more rapidly, on the high-shear region at the poles, and it is highly suggestive of the nature of the eroded shape and locations of regularity loss to come.

As a second problem we again begin with a spherical particle centered at the origin, but now we take background velocity $\mathbf{u}^\infty(\mathbf{x}) = (x_3 + \kappa)\hat{\mathbf{x}}_1$ so that the sphere center lies a distance κ above the plane of zero background flow. For $\kappa > 1$ the background flow is everywhere in the positive x_1 -direction over the body surface, and the flow is stronger at the top of the particle. The particle evolution is shown in the second row of Fig. 6 and a series of outlines are plotted in Fig. 7(b). The most dramatic change compared to the more symmetric configuration considered above is the absence of corners in the profile viewed along the x_1 -direction; i.e. the second column of Fig. 7 has fewer sharp corners than the first. To better understand the shape evolution we again look to the exact velocity and traction fields at $t = 0$. The exact velocity and traction fields at $t = 0$ are found by adding to (37) the flow due to a Stokeslet and source dipole, resulting in the fluid velocity

$$u_i(\mathbf{x}) = \left(\frac{1}{2} - \frac{a^3}{2r^3}\right)\epsilon_{i2k}x_k + \left(\frac{1}{2} - \frac{a^5}{2r^5}\right)s_{ij}x_j + \left(\frac{5a^5}{4r^7} - \frac{5a^3}{4r^5}\right)x_i x_j x_k s_{jk} + \kappa\delta_{1i}\left(1 - \frac{3}{4}\left(\frac{a}{r} + \frac{a^3}{3r^3}\right)\right) - \frac{3\kappa a}{4}\frac{x_1 x_i}{r^3}\left(1 - \frac{a^2}{r^2}\right). \quad (43)$$

This flow field is depicted in Fig. 8b for $\kappa = 1.5, a = 1$ along with the contours of the (exact) tangential

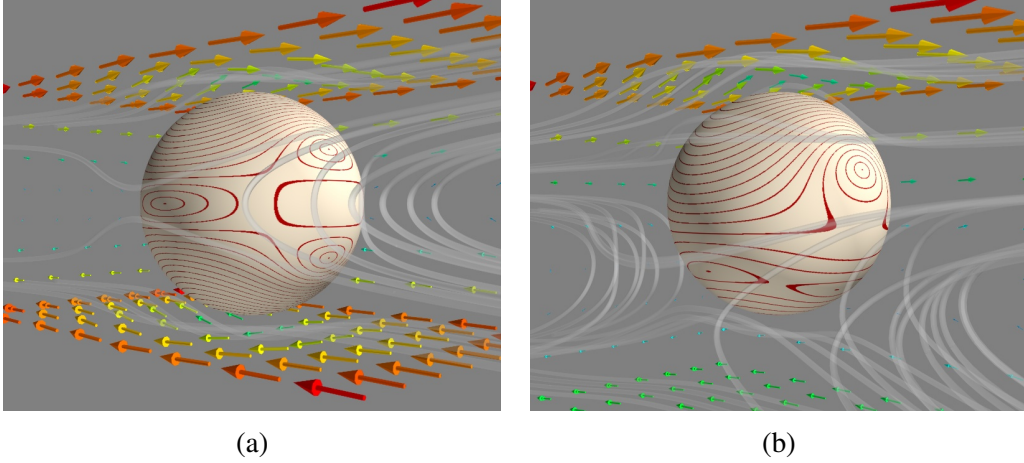


FIG. 8. Exact flow fields and surface tractions for a sphere held fixed (a) with the plane of zero background flow through the sphere center, and (b) with the plane of zero background flow located 1.5 radii below the sphere center (as in the first two rows of Fig. 6). Contours of the shear stress magnitude, $|(\mathbf{I} - \mathbf{n}\mathbf{n}) \cdot \mathbf{f}|$ are shown in red on the spherical surface. In both cases we see regions of recirculating flow (lower in (b) than in (a)), and in both cases the locations of zero shear stress are stagnation points for the flow, resulting in an impending loss of surface smoothness.

stress on the particle surface. As expected, the top half of the sphere has a large shear stress although there are two small regions of reduced shear stress surrounding the two stagnation points which lie on the upper hemisphere. The locations of the stagnation points in the neutral $\{x_2 = 0\}$ plane can again be obtained algebraically as $(\pm \cos(\phi), 0, \sin(\phi))$ where

$$\sin(\phi) = \frac{-3}{20}\kappa \pm \frac{1}{20}\sqrt{9\kappa^2 + 80}. \quad (44)$$

For $\kappa < 8/3$, both choices of sign in (44) lead to real arcsines and there is a recirculation region in the flow; in this case the lower half of the sphere has a region of moderate tangential stress at the pole and a stagnation point where the incoming flow divides. It is interesting that for κ in this range the fluid immediately below the body moves in the negative x_1 -direction although the background flow there was in the positive x_1 -direction. As in the previous case, this detailed description of the initial flow field predicts effectively the subsequent evolution, as depicted in Fig. 6 and with outlines given in Fig. 7. In particular, we note the persistence of the recirculation region against the lower portion of the body, separated by corners from the rapidly ablating zone on the upper hemisphere and from the smaller and more slowly ablating region near the lower pole.

Finally, we consider a background shear flow above a plane wall. The center of the initially spherical particle is placed at $(0, 0, 1.5)$, the background flow is given by $\mathbf{u}^\infty(\mathbf{x}) = x_3\hat{\mathbf{x}}_1$, and we impose a no-slip condition on the wall at $\{x_3 = 0\}$. The exact flow fields and tractions are not so convenient here, but it is known that the flow between the sphere and the wall is slow and in the positive x_1 -direction, so there is no recirculation region and only one stagnation point pair (they appear in pairs because of the fore-aft symmetry) [92, Fig 2]. The resulting evolution, depicted in the third row of Fig. 6 and with outlines in Fig. 7(c), accordingly results in a geometry with only one pair of cusps, in contrast to the greater numbers observed in the previous cases. In particular, the inclusion of a wall results in slower flow and a smoother, more spherical body shape there as the particle erodes toward oblivion.

VI. CONCLUSION

We used the Lorentz reciprocal theorem to derive a completed traction boundary integral equation which allows for the incorporation of background and/or wall-bounded flows. Integrals involving the background velocity and its stress field were performed on an imaginary bounding sphere or hemisphere, and the integration was carried out exactly for the case of linear background flows. We used the method to study two applications, first to investigate at a greater level of detail the tractions on glancing and reversing trajectories of ellipsoids near a wall, and then to study the erosion of bodies by a viscous flow wherein the surface is ablated at a rate proportional to the local viscous shear stress. Sharp corners were found to develop at stagnation points. Moreover, the full evolution of the particle geometry can be largely predicted from an understanding of the flow past the initial shape. These features of viscous erosion are expected to be generic and observable for more complicated initial body geometries. An initially spherical body was found to reduce to a shape reminiscent of Pironneau’s drag-minimizing profile, but we then showed that a self-similar reduction of an axisymmetric body under constant shear stress occurs only for a sphere or a cone. The body was found to vanish in finite time with a power law scaling of $(t - t_f)^{1/2}$, in contrast to the 4/3 power law scaling observed at high Reynolds number [51]. The presence of a nearby wall was found to have a smoothing effect, as it reduced the number of stagnation points appearing on the initial body surface.

The boundary integral equation presented here addresses any background flow $(\mathbf{u}^\infty, p^\infty)$ satisfying $-\nabla p^\infty + \mu \nabla^2 \mathbf{u}^\infty = \mathbf{0}$ and $\nabla \cdot \mathbf{u}^\infty = 0$ throughout the fluid domain. That is, we have considered the everywhere regular Stokes background flows. The restriction to regular Stokes flows is not essential and our argument can be extended to cover, *e.g.*, the problem of finding the tractions on a rigid body which translates with specified velocity near a point source or a point force. The extension to several particles is also straightforward.

We found an especially convenient formula in the case of linear background flows; it would be valuable to carry out these computations for the case of flows with higher moments as well. A greater and more long-term project is to remove the restriction to rigid-body motion. This is a more profound mathematical challenge because the rigid-body hypothesis is needed for the essential equation (18). In the meantime, problems involving bodies which are changing shape only slowly relative to a background velocity field might be effectively handled in a quasi-steady manner, as we have pursued for the problem of viscous erosion. Other directions of current investigation include studying the shape dynamics and associated trajectories of force- and torque-free eroding bodies, and a more detailed analysis of non-smooth surfaces. The low Reynolds number analogue of the process of melting or dissolution in flow, independent of shear stress [56], is another appealing direction for future study.

VII. ACKNOWLEDGEMENTS

We gratefully acknowledge helpful conversations with Nick Moore and Gwynn Elfring. Funding for this research was provided by the NSF (grant number DMS-1056327) and the Wisconsin Alumni Research Foundation.

Appendix A: Formulas for fundamental singularities in a half-space

Formulas for the fundamental solutions of the Stokes equations in a half-space have been derived elsewhere by various means: using the Lorentz reflection procedure [79, 85], a Fourier argument [97, 98], brute-force differentiation [99], and a Papkovitch-Neuber potential [100]. In this paper we use formulas obtained following the Lorentz method. The procedure is as follows. Given a flow (\mathbf{u}, p) which satisfies the Stokes system on all of \mathbb{R}^3 except at a source point \mathbf{y} above a plane wall at $\{x_3 = 0\}$, we define two new

solutions (\mathbf{v}, q) and (\mathbf{u}^*, p^*) via

$$v_i = -\beta_{ij}u_j - 2x_3 \frac{\partial u_3}{\partial x_i} + x_3^2 \nabla^2 u_i, \quad q = p + 2x_3 \frac{\partial p}{\partial x_3} - 4 \frac{\partial u_3}{\partial x_3}, \quad (\text{A1})$$

and

$$u_i^*(\mathbf{x}) = \beta_{ij}v_j(\beta\mathbf{x}), \quad p^*(\mathbf{x}) = q(\beta\mathbf{x}). \quad (\text{A2})$$

Here $\beta_{ij} = \delta_{ij} - 2\delta_{3i}\delta_{3j}$ denotes the operator of reflection over the wall. Both (\mathbf{v}, q) and (\mathbf{u}^*, p^*) are solutions of the Stokes equations, and moreover the latter flow is the required correction to \mathbf{u} on the wall: $(\mathbf{u} + \mathbf{u}^*, p + p^*)$ satisfies the no-slip condition at $\{x_3 = 0\}$ and has the same singular behavior as (\mathbf{u}, p) at the source point. Applying these formulas to the point force, point torque, and stresslet given in Table I, and then simplifying to reduce the algebraic operations required to evaluate the formulas, we obtain the wall-bounded tensors printed in Table III. We are not aware of any previously published expression for the stress field of the wall-bounded stresslet.

Appendix B: Useful integration identities

The integrals on the right-hand side of (23) may be evaluated using the identities

$$\int_S \frac{x_i x_j}{|\mathbf{x}|^4} dS_{\mathbf{x}} = \frac{4\pi}{3} \delta_{ij}, \quad (\text{B1})$$

$$\int_S \frac{x_i x_j x_k x_\ell}{|\mathbf{x}|^6} dS_{\mathbf{x}} = \frac{4\pi}{15} (\delta_{ij}\delta_{k\ell} + \delta_{ik}\delta_{j\ell} + \delta_{il}\delta_{jk}), \quad (\text{B2})$$

$$\frac{1}{|\mathbf{x} - \mathbf{y}|^p} = \frac{1}{|\mathbf{x}|^p} + p \frac{x_i y_i}{|\mathbf{x}|^{p+2}} + \mathcal{O}(1/|\mathbf{x}|^{p+2}). \quad (\text{B3})$$

For a linear background flow, $u^\infty(\mathbf{x}) = A\mathbf{x}$, in the limit where the radius of S increases to infinity, we have

$$\frac{\mu}{8\pi} \int_S u_i^\infty(\mathbf{x}) \hat{n}_m(\mathbf{x}) T_{ijkm}^{STR}(\mathbf{x}, \mathbf{y}) n_k(\mathbf{y}) dS_{\mathbf{x}} = \frac{-3\mu}{5} (A_{jk} + A_{kj}) n_k(\mathbf{y}), \quad (\text{B4})$$

$$\frac{c\mu}{8\pi} \int_S u_i^\infty(\mathbf{x}) \hat{n}_m(\mathbf{x}) C_{ijm}^{STR}(\mathbf{x}, \mathbf{y}) dS_{\mathbf{x}} = \frac{3c\mu}{10} (A_{jk} + A_{kj}) z_k(\mathbf{y}) + \frac{c\mu}{2} (A_{jk} - A_{kj}) y_k, \quad (\text{B5})$$

$$-\frac{1}{8\pi} \int_S f_i^\infty(\mathbf{x}) T_{ijk}(\mathbf{x}, \mathbf{y}) n_k(\mathbf{y}) dS_{\mathbf{x}} = \frac{-2\mu}{5} (A_{jk} + A_{kj}) n_k(\mathbf{y}), \quad (\text{B6})$$

$$-\frac{c}{8\pi} \int_S f_i^\infty(\mathbf{x}) C_{ij}(\mathbf{x}, \mathbf{y}) dS_{\mathbf{x}} = \frac{c\mu}{5} (A_{jk} + A_{kj}) z_k(\mathbf{y}). \quad (\text{B7})$$

-
- [1] C. Picioreanu, M. C. M. Van Loosdrecht, J. J. Heijnen, et al. Two-dimensional model of biofilm detachment caused by internal stress from liquid flow. *Biotech. & Bioeng.*, 72(2):205–218, 2001.
 - [2] Y. Liu and J.-H. Tay. The essential role of hydrodynamic shear force in the formation of biofilm and granular sludge. *Water Res.*, 36(7):1653–1665, 2002.
 - [3] P. Stoodley, R. Cargo, C.J. Rupp, S. Wilson, and I. Klapper. Biofilm material properties as related to shear-induced deformation and detachment phenomena. *J. Ind. Microbiol. Biotechnol.*, 29(6):361–367, 2002.
 - [4] R. M. Donlan and J. W. Costerton. Biofilms: survival mechanisms of clinically relevant microorganisms. *Clin. Microbiol. Rev.*, 15(2):167–193, 2002.

Stokeslet velocity G_{ij}^{half}	$\frac{\delta_{ij}}{R} - \frac{\delta_{ij}}{\hat{R}} + \frac{X_i X_j}{R^3} - \frac{X_i X_j}{\hat{R}^3} - \frac{2\delta_{ij} y_3 x_3}{\hat{R}^3} + \frac{6y_3 x_3 \hat{X}_j \beta_{il} \hat{X}_l}{\hat{R}^5}$
Stokeslet pressure $G_j^{\text{half}, P}$	$2\frac{X_j}{R^3} - 2\frac{X_j}{\hat{R}^3} - 12Y_3 \frac{\hat{X}_3 \hat{X}_j}{\hat{R}^5}$
Stokeslet stress $G_{ijk}^{\text{half}, STR}$	$-6\frac{X_i X_j X_m}{R^5} + \frac{6}{\hat{R}^5} \left[X_i X_j X_m - 2\delta_{im} y_3^2 \hat{X}_j + \delta_{3m} y_3 (X_i X_j + \beta_{it} \hat{X}_t \hat{X}_j) + \delta_{3i} y_3 (X_j X_m + \hat{X}_j \beta_{mt} \hat{X}_t) \right. \\ \left. + x_3 y_3 (\delta_{ij} \beta_{mt} + \delta_{jm} \beta_{it} + \beta_{jm} \beta_{it} + \beta_{ij} \beta_{mt}) \hat{X}_t \right] - 30 \frac{x_3 y_3 \hat{X}_j (\beta_{it} \beta_{mt} + \beta_{mt} \beta_{it}) \hat{X}_l \hat{X}_t}{\hat{R}^7}$
rotlet velocity R_{im}^{half}	$\frac{\epsilon_{imk} X_k}{R^3} - \frac{\epsilon_{imk} X_k}{\hat{R}^3} - \frac{6\epsilon_{3mk} \hat{X}_k x_3 \beta_{il} \hat{X}_l}{\hat{R}^5}$
rotlet pressure $R_m^{\text{half}, P}$	$12 \frac{\epsilon_{3mk} \hat{X}_k \hat{X}_3}{\hat{R}^5}$
rotlet stress $R_{imp}^{\text{half}, STR}$	$-3 \frac{\epsilon_{imk} X_k X_p + \epsilon_{pmk} X_k X_i}{R^5} + \frac{60}{\hat{R}^7} x_3 \beta_{il} \hat{X}_l \epsilon_{3mk} \hat{X}_k \beta_{ps} \hat{X}_s + \frac{3}{\hat{R}^5} (\epsilon_{imk} \hat{X}_k \beta_{ps} \hat{X}_s + \epsilon_{pmk} \hat{X}_k \beta_{is} \hat{X}_s + 2x_3 \epsilon_{im3} \beta_{ps} \hat{X}_s \\ + 2x_3 \epsilon_{pm3} \beta_{is} \hat{X}_s - 2\delta_{3p} \beta_{il} \hat{X}_l \epsilon_{3mk} \hat{X}_k - 2\delta_{3i} \beta_{pl} \hat{X}_l \epsilon_{3mk} \hat{X}_k + 4y_3 \delta_{ip} \epsilon_{3mk} \hat{X}_k - 2x_3 \beta_{il} \hat{X}_l \epsilon_{3mp} - 2x_3 \beta_{pl} \hat{X}_l \epsilon_{3mi})$
stresslet velocity T_{ijk}^{half}	$-6\frac{X_i X_j X_k}{R^5} + 6\frac{X_i \hat{X}_j \hat{X}_k}{\hat{R}^5} - \frac{12x_3 (\delta_{jk} \beta_{im} \hat{X}_m - y_3 \beta_{ik} \hat{X}_j - y_3 \beta_{ij} \hat{X}_k)}{\hat{R}^5} - 60x_3 y_3 \frac{\hat{X}_j \hat{X}_k \beta_{im} \hat{X}_m}{\hat{R}^7}$
stresslet pressure $T_{jk}^{\text{half}, P}$	$4\delta_{jk} \left(\frac{1}{R^3} + \frac{1}{\hat{R}^3} \right) - 12\frac{X_j X_k}{R^5} + 12\frac{\hat{X}_j \hat{X}_k}{\hat{R}^5} - 24y_3 \frac{\delta_{3k} \hat{X}_j + \delta_{3j} \hat{X}_k}{\hat{R}^5} + 24\delta_{jk} \frac{x_3 \hat{X}_3}{\hat{R}^5} + 120y_3 \frac{\hat{X}_3 \hat{X}_j \hat{X}_k}{\hat{R}^7}$
stresslet stress $T_{ijkm}^{\text{half}, STR}$	$-4\delta_{im} \delta_{jk} \left(\frac{1}{R^3} + \frac{1}{\hat{R}^3} \right) - \frac{6}{R^5} (\delta_{ij} X_k X_m + \delta_{ik} X_j X_m + \delta_{jm} X_i X_k + \delta_{km} X_i X_j) + \frac{60}{R^7} X_i X_j X_k X_m \\ + \frac{6}{\hat{R}^5} [4\delta_{im} y_3 (\delta_{3k} \hat{X}_j + \delta_{3j} \hat{X}_k) + 4x_3 y_3 (\delta_{im} \delta_{jk} + \beta_{ik} \beta_{jm} + \beta_{ij} \beta_{km}) + \beta_{it} \hat{X}_t (\beta_{jm} \hat{X}_k + \beta_{km} \hat{X}_j - 4\delta_{3m} x_3 \delta_{jk}) \\ + \beta_{mt} \hat{X}_t (\beta_{ij} \hat{X}_k + \beta_{ik} \hat{X}_j - 4\delta_{3i} x_3 \delta_{jk})] + \frac{60}{\hat{R}^7} [2\delta_{im} y_3^2 \hat{X}_j \hat{X}_k + 2\delta_{jk} x_3^2 \beta_{it} \hat{X}_t \beta_{mp} \hat{X}_p - \hat{X}_j \hat{X}_k \beta_{it} \hat{X}_t \beta_{mp} \hat{X}_p \\ - 2x_3 y_3 \beta_{mp} \hat{X}_p (\beta_{ik} \hat{X}_j + \beta_{ij} \hat{X}_k) - 2x_3 y_3 \beta_{it} \hat{X}_t (\beta_{km} \hat{X}_j + \beta_{jm} \hat{X}_k)] + \frac{840}{\hat{R}^9} x_3 y_3 \hat{X}_j \hat{X}_k \beta_{it} \hat{X}_t \beta_{mp} \hat{X}_p$

TABLE III. Formulas for three singularity solutions of the Stokes equations in a fluid with no-slip boundary at $\{x_3 = 0\}$. Here $\mathbf{X} = \mathbf{x} - \mathbf{y}$ where \mathbf{x} is the observation point and \mathbf{y} is the location of the singularity above the wall. We write $\beta_{ij} = \delta_{ij} - 2\delta_{3i}\delta_{3j}$ for the reflection operator and $\hat{X}_i = \beta_{ij}x_j - y_i$. In the denominators we have written $R = |\mathbf{X}|$ and $\hat{R} = |\hat{\mathbf{X}}|$. It is interesting that the velocity tensor of the stresslet does not match the stress tensor of the stokeslet as in free space; indeed the stress tensor of the wall-bounded stokeslet does not vanish on the wall.

- [5] M. Simoes, M. O. Pereira, and M. J. Vieira. Effect of mechanical stress on biofilms challenged by different chemicals. *Water Res.*, 39(20):5142–5152, 2005.
- [6] M. R. Nejadnik, H. C. van der Mei, W. Norde, and H. J. Busscher. Bacterial adhesion and growth on a polymer brush-coating. *Biomaterials*, 29(30):4117–4121, 2008.
- [7] G. W. Schmid-Schönbein. Biomechanics of microcirculatory blood perfusion. *Annu. Rev. Biomedical Eng.*, 1(1):73–102, 1999.
- [8] P. J. Butler, G. Norwich, S. Weinbaum, and S. Chien. Shear stress induces a time- and position-dependent increase in endothelial cell membrane fluidity. *Am. J. Phys.-Cell Phys.*, 280(4):C962–C969, 2001.
- [9] P. F. Davies, A. Remuzzi, E. J. Gordon, C. F. Dewey, and M. A. Gimbrone. Turbulent fluid shear stress induces vascular endothelial cell turnover in vitro. *Proc. Natl. Acad. Sci. USA*, 83(7):2114–2117, 1986.

- [10] Z.M. Ruggeri, J. N. Orje, R. Habermann, A. B. Federici, and A. J. Reininger. Activation-independent platelet adhesion and aggregation under elevated shear stress. *Blood*, 108(6):1903–1910, 2006.
- [11] P. K. Shah. Pathophysiology of coronary thrombosis: role of plaque rupture and plaque erosion. *Prog. Cardiovasc. Dis.*, 44:357–368, 2002.
- [12] H. C. Groen, F. J. H. Gijzen, A. van der Lugt, M. S. Ferguson, T. S. Hatsukami, A. F. W. van der Steen, C. Yuan, and J. J. Wentzel. Plaque rupture in the carotid artery is localized at the high shear stress region a case report. *Stroke*, 38:2379–2381, 2007.
- [13] R. M. Hochmuth, N. Mohandas, and PL Blackshear Jr. Measurement of the elastic modulus for red cell membrane using a fluid mechanical technique. *Biophys. J.*, 13(8):747, 1973.
- [14] T. R. Powers. Dynamics of filaments and membranes in a viscous fluid. *Rev. Mod. Phys.*, 82(2):1607, 2010.
- [15] H. Stone and C. Duprat. Model problems coupling elastic boundaries and viscous flows. *Fluid-Structure Interactions in Low-Reynolds-Number Flows*, page 78, 2015.
- [16] E. J. Hinch. The deformation of a nearly straight thread in a shearing flow with weak brownian motions. *J. Fluid Mech.*, 75(04):765–775, 1976.
- [17] L. E. Becker and M. J. Shelley. Instability of elastic filaments in shear flow yields first-normal-stress differences. *Phys. Rev. Lett.*, 87(19):198301, 2001.
- [18] A.-K. Tornberg and M. J. Shelley. Simulating the dynamics and interactions of flexible fibers in stokes flows. *J. Comput. Phys.*, 196(1):8–40, 2004.
- [19] V. Kantsler and R. E. Goldstein. Fluctuations, dynamics, and the stretch-coil transition of single actin filaments in extensional flows. *Phys. Rev. Lett.*, 108(3):038103, 2012.
- [20] L. Li, H. Manikantan, D. Saintillan, and S. E. Spagnolie. The sedimentation of flexible filaments. *J. Fluid Mech.*, 735:705–736, 2013.
- [21] A. Lindner and M. Shelley. Elastic fibers in flows. *Fluid-Structure Interactions in Low-Reynolds-Number Flows*, page 168, 2015.
- [22] H. Manikantan and D. Saintillan. Buckling transition of a semiflexible filament in extensional flow. *Physical Review E*, 92(4):041002, 2015.
- [23] M. Kraus, W. Wintz, U. Seifert, and R. Lipowsky. Fluid vesicles in shear flow. *Phys. Rev. Lett.*, 77(17):3685, 1996.
- [24] M. Abkarian and A. Viallat. Dynamics of vesicles in a wall-bounded shear flow. *Biophys. J.*, 89(2):1055–1066, 2005.
- [25] V. Kantsler and V. Steinberg. Transition to tumbling and two regimes of tumbling motion of a vesicle in shear flow. *Phys. Rev. Lett.*, 96(3):036001, 2006.
- [26] H. Noguchi and G. Gompper. Swinging and tumbling of fluid vesicles in shear flow. *Phys. Rev. Lett.*, 98(12):128103, 2007.
- [27] S. K. Veerapaneni, D. Gueyffier, G. Biros, and D. Zorin. A numerical method for simulating the dynamics of 3D axisymmetric vesicles suspended in viscous flows. *J. Comput. Phys.*, 228(19):7233–7249, 2009.
- [28] C. Pozrikidis. Numerical simulation of the flow-induced deformation of red blood cells. *Ann. Biomed. Eng.*, 31(10):1194–1205, 2003.
- [29] B. Kaoui, G. Biros, and C. Misbah. Why do red blood cells have asymmetric shapes even in a symmetric flow? *Phys. Rev. Lett.*, 103(18):188101, 2009.
- [30] Z. Peng, R. J. Asaro, and Q. Zhu. Multiscale modelling of erythrocytes in Stokes flow. *J. Fluid Mech.*, 686:299–337, 2011.
- [31] X. Li, P. M. Vlahovska, and G. E. Karniadakis. Continuum-and particle-based modeling of shapes and dynamics of red blood cells in health and disease. *Soft Matter*, 9(1):28–37, 2013.
- [32] S. K. Veerapaneni, D. Gueyffier, D. Zorin, and G. Biros. A boundary integral method for simulating the dynamics of inextensible vesicles suspended in a viscous fluid in 2D. *J. Comput. Phys.*, 228(7):2334–2353, 2009.
- [33] A. Rahimian, I. Lashuk, S. Veerapaneni, A. Chandramowlishwaran, D. Malhotra, L. Moon, R. Sampath, A. Shringarpure, J. Vetter, R. Vuduc, et al. Petascale direct numerical simulation of blood flow on 200k cores and heterogeneous architectures. In *Proceedings of the 2010 ACM/IEEE International Conference for High Performance Computing, Networking, Storage and Analysis*, pages 1–11. IEEE Computer Society, 2010.
- [34] A. Kumar and M. D. Graham. Margination and segregation in confined flows of blood and other multicomponent suspensions. *Soft Matter*, 8(41):10536–10548, 2012.
- [35] J. B. Freund. Numerical simulation of flowing blood cells. *Annu. Rev. Fluid Mech.*, 46:67–95, 2014.

- [36] D. A. Fedosov, H. Noguchi, and G. Gompper. Multiscale modeling of blood flow: from single cells to blood rheology. *Biomech. Model. Mechanobiol.*, 13(2):239–258, 2014.
- [37] A. Kumar and M. D. Graham. Cell distribution and segregation phenomena during blood flow. In *Complex Fluids in Biological Systems*, pages 399–435. Springer, 2015.
- [38] S. Sukumaran and U. Seifert. Influence of shear flow on vesicles near a wall: a numerical study. *Phys. Rev. E*, 64(1):011916, 2001.
- [39] H. Zhao, A. P. Spann, and E. S. G. Shaqfeh. The dynamics of a vesicle in a wall-bound shear flow. *Phys. Fluids*, 23(12):121901, 2011.
- [40] E. Lauga and T.R. Powers. The hydrodynamics of swimming microorganisms. *Rep. Prog. Phys.*, 72:096601, 2009.
- [41] S. R. Keller, T. Y. Wu, and C. Brennen. A traction-layer model for ciliary propulsion. In *Swimming and Flying in Nature (Wu, T. Y., Brokaw, C. J. & Brennen, C. J. eds.)*, pages 253–271. Plenum Press, 1975.
- [42] M. A. Sleight, J. R. Blake, and N. Liron. The propulsion of mucus by cilia. *Am. Rev. Respir. Dis.*, 137(3):726–741, 1988.
- [43] A. Kanevsky, M. J. Shelley, and A.-K. Tornberg. Modeling simple locomotors in stokes flow. *J. Comput. Phys.*, 229(4):958–977, 2010.
- [44] S. Michelin and E. Lauga. Efficiency optimization and symmetry-breaking in a model of ciliary locomotion. *Phys. Fluids*, 22(11):111901, 2010.
- [45] S. Childress. *Mechanics of swimming and flying*, volume 2. Cambridge University Press, 1981.
- [46] S. Jana, S. H. Um, and S. Jung. Paramecium swimming in capillary tube. *Phys. Fluids*, 24(4):041901, 2012.
- [47] L. Zhu, E. Lauga, and L. Brandt. Low-Reynolds-number swimming in a capillary tube. *J. Fluid Mech.*, 726:285–311, 2013.
- [48] L. Li and S. E. Spagnolie. Swimming and pumping by helical waves in viscous and viscoelastic fluids. *Phys. Fluids*, 27(2):021902, 2015.
- [49] S. E. Spagnolie and E. Lauga. Jet propulsion without inertia. *Phys. Fluids*, 22(8):081902, 2010.
- [50] L. Ristroph, M. N. J. Moore, S. Childress, M. J. Shelley, and J. Zhang. Sculpting of an erodible body by flowing water. *Proc. Natl. Acad. Sci. USA*, 109(48):19606–19609, 2012.
- [51] M. N. J. Moore, L. Ristroph, S. Childress, J. Zhang, and M. J. Shelley. Self-similar evolution of a body eroding in a fluid flow. *Phys. Fluids*, 25(11):116602, 2013.
- [52] J. Mac Huang, M. N. J. Moore, and L. Ristroph. Shape dynamics and scaling laws for a body dissolving in fluid flow. *J. Fluid Mech.*, 765:R3, 2015.
- [53] F. H. Garner and R. W. Grafton. Mass transfer in fluid flow from a solid sphere. *Proc. Roy. Soc. Lond. A*, 224(1156):64–82, 1954.
- [54] T. J. Hanratty. Stability of surfaces that are dissolving or being formed by convective diffusion. *Annu. Rev. Fluid Mech.*, 13(1):231–252, 1981.
- [55] G. Daccord and R. Lenormand. Fractal patterns from chemical dissolution. *Nature*, 325(6099):41–43, 1987.
- [56] C. H. Rycroft and M. Z. Bazant. Asymmetric collapse by dissolution or melting in a uniform flow. In *Proc. Roy. Soc. A Lond.*, volume 472, page 20150531. The Royal Society, 2016.
- [57] YL Hao and Y-X Tao. Heat transfer characteristics of melting ice spheres under forced and mixed convection. *J. Heat Transfer*, 124(5):891–903, 2002.
- [58] A. Kumar and S. Roy. Heat transfer characteristics during melting of a metal spherical particle in its own liquid. *Int. J. Therm. Sci.*, 49(2):397–408, 2010.
- [59] F. H. Garner and R. B. Keey. Mass-transfer from single solid spheres I: Transfer at low Reynolds numbers. *Chem. Eng. Sci.*, 9(2):119–129, 1958.
- [60] M. Linton and K. L. Sutherland. Transfer from a sphere into a fluid in laminar flow. *Chem. Eng. Sci.*, 12(3):214–229, 1960.
- [61] R. L. Steinberger and R. E. Treybal. Mass transfer from a solid soluble sphere to a flowing liquid stream. *AIChE J.*, 6(2):227–232, 1960.
- [62] R. W. Grafton. Prediction of mass transfer from spheres and cylinders in forced convection. *Chem. Eng. Sci.*, 18(7):457–466, 1963.
- [63] A. C. Lochiel and P. H. Calderbank. Mass transfer in the continuous phase around axisymmetric bodies of revolution. *Chem. Eng. Sci.*, 19(7):471–484, 1964.
- [64] K. Aminzadeh, T. R. Al Taha, A. R. H. Cornish, M. S. Kolansky, and R. Pfeffer. Mass transport around two spheres at low Reynolds numbers. *Int. J. Heat Mass Tran.*, 17(12):1425–1436, 1974.

- [65] A. A. Jeschke and W. Dreybrodt. Dissolution rates of minerals and their relation to surface morphology. *Geochim. Cosmochim. Acta*, 66(17):3055–3062, 2002.
- [66] J. Colombani. Measurement of the pure dissolution rate constant of a mineral in water. *Geochim. Cosmochim. Acta*, 72(23):5634–5640, 2008.
- [67] M. M. Mbogoro, M. E. Snowden, M. A. Edwards, M. Peruffo, and P. R. Unwin. Intrinsic kinetics of gypsum and calcium sulfate anhydrite dissolution: surface selective studies under hydrodynamic control and the effect of additives. *Phys. Chem. C*, 115(20):10147–10154, 2011.
- [68] K. G. Nelson and A. C. Shah. Convective diffusion model for a transport-controlled dissolution rate process. *J. Pharma. Sci.*, 64(4):610–614, 1975.
- [69] H. Grijseels, D. J. A. Crommelin, and C. J. De Blaey. Hydrodynamic approach to dissolution rate. *Pharm. Weekbl. Sci.*, 3(1):1005–1020, 1981.
- [70] V. Pillay and R. Fassihi. Unconventional dissolution methodologies. *J. Pharma. Sci.*, 88(9):843–851, 1999.
- [71] P. J. Missel, L. E. Stevens, and J. W. Mauger. Reexamination of convective diffusion/drug dissolution in a laminar flow channel: accurate prediction of dissolution rate. *Pharmaceut. Res.*, 21(12):2300–2306, 2004.
- [72] A. Dokoumetzidis and P. Macheras. A century of dissolution research: from Noyes and Whitney to the biopharmaceutics classification system. *Int. J. Pharm.*, 321(1):1–11, 2006.
- [73] D. M. D’Arcy, O. I. Corrigan, and A. M. Healy. Evaluation of hydrodynamics in the basket dissolution apparatus using computational fluid dynamics - dissolution rate implications. *European J. Pharma. Sci.*, 27(2):259–267, 2006.
- [74] G. E. Bai and P. M. Armenante. Hydrodynamic, mass transfer, and dissolution effects induced by tablet location during dissolution testing. *J. Pharma. Sci.*, 98(4):1511–1531, 2009.
- [75] I. Stakgold and M. J. Holst. *Green’s functions and boundary value problems*, volume 99. John Wiley & Sons, 2011.
- [76] G. K. Youngren and A. Acrivos. Stokes flow past a particle of arbitrary shape: a numerical method of solution. *J. Fluid Mech.*, 69(02):377–403, 1975.
- [77] H. Power and G. Miranda. Second kind integral equation formulation of Stokes’ flows past a particle of arbitrary shape. *SIAM J. Appl. Math.*, 47(4):689–698, 1987.
- [78] E. E. Keaveny and M. J. Shelley. Applying a second-kind boundary integral equation for surface tractions in Stokes flow. *J. Comput. Phys.*, 230(5):2141–2159, 2011.
- [79] S. Kim and S.J. Karrila. *Microhydrodynamics: Principles and Selected Applications*. Dover Publications, Inc., Mineola, NY, 1991.
- [80] N. Liron and E. Barta. Motion of a rigid particle in Stokes flow: a new second-kind boundary-integral equation formulation. *J. Fluid Mech.*, 238:579–598, 1992.
- [81] M. S. Ingber and L.A. Mondy. Direct second kind boundary integral formulation for Stokes flow problems. *Comput. Mech.*, 11(1):11–27, 1993.
- [82] C. Pozrikidis. Shear flow over a protuberance on a plane wall. *J. Eng. Math.*, 31(6):29–42, 1997.
- [83] G.K. Batchelor. *Introduction to Fluid Dynamics*. Cambridge University Press, Cambridge, England, 1967.
- [84] H. K. Kuiken. HA Lorentz: Sketches of his work on slow viscous flow and some other areas in fluid mechanics and the background against which it arose. *J. Engr. Math.*, 30:1–18, 1996.
- [85] H.A. Lorentz. Eene algemeene stelling omtrent de beweging eener vloeistof met wrijving en eenige daaruit afgeleide gevolgen. *Zittingsverslag van de Koninklijke Akademie van Wetenschappen te Amsterdam*, (5):168–175, 1896.
- [86] C. Pozrikidis. *Boundary integral and singularity methods for linearized viscous flow*. Cambridge University Press, 1992.
- [87] H.A. Lorentz. Ein allgemeiner satz, die bewegung einer reibenden flüssigkeit betreffend, nebst einigen anwendungen desselben. *Abhand. Theor. Phys. (Leipzig)*, (1):23–42, 1907.
- [88] G Strang and PO Persson. A simple mesh generator in matlab. *SIAM Rev*, 46(2):329–345, 2004.
- [89] Y. Saad and M. H. Schultz. GMRES: A generalized minimal residual algorithm for solving nonsymmetric linear systems. *SIAM J. Sci. Stat. Comp.*, 7:856–869, 1986.
- [90] A. J. Goldman, R. G. Cox, and H. Brenner. Slow viscous motion of a sphere parallel to a plane wall - I motion through a quiescent fluid. *Chem. Eng. Sci.*, 22(4):637–651, 1967.
- [91] M. E. O’Neill and B. S. Bhatt. Slow motion of a solid sphere in the presence of a naturally permeable surface. *Q. J. Mech. Appl. Math.*, 44(1):91–104, 1991.
- [92] M. Chaoui and F. Feuillebois. Creeping flow around a sphere in a shear flow close to a wall. *Q. J. Mech. Appl. Math.*, 56(3):381–410, 2003.

- [93] W. H. Mitchell and S. E. Spagnolie. Sedimentation of spheroidal bodies near walls in viscous fluids: glancing, reversing, tumbling and sliding. *J. Fluid Mech.*, 772:600–629, 2015.
- [94] S. Kim. Ellipsoidal microhydrodynamics without elliptic integrals and how to get there using linear operator theory: A note on weighted inner products. *Ind. Eng. Chem. Res.*, 54(42):10549–10551, 2015.
- [95] O. Pironneau. On optimal profiles in Stokes flow. *J. Fluid Mech.*, 59:117–128, 1973.
- [96] J.-M. Bourot. On the numerical computation of the optimum profile in Stokes flow. *J. Fluid Mech.*, 65:513–515, 1974.
- [97] J.R. Blake. A note on the image system for a Stokeslet in a no-slip boundary. *Math. Proc. Cambridge*, 70:303–310, 1971.
- [98] J. R. Blake and A. T. Chwang. Fundamental singularities of viscous flow. *J. Eng. Math.*, 8(1):23–29, 1974.
- [99] S.E. Spagnolie and E. Lauga. Hydrodynamics of self-propulsion near boundaries: predictions and accuracy of far-field approximations. *J. Fluid. Mech.*, pages 1–43, 2012.
- [100] Z. Gimbutas, L. Greengard, and S. Veerapaneni. Simple and efficient representations for the fundamental solutions of Stokes flow in a half-space. *J. Fluid Mech.*, 776, 8 2015.